Check for updates

Global Biogeochemical Cycles®

AGU ADVANCING EARTH AND SPACE SCIENCES

RESEARCH ARTICLE

Key Points:

- The Indian Ocean pH is decreasing at an average rate of 0.015 dec^{-1} from 1980 to 2019
- The trend of dissolved inorganic carbon primarily drives an increasing ocean acidification trend in the Indian Ocean
- El Niño and positive Indian Ocean Dipole events lead to an enhancement of the Indian Ocean acidification

Author Contributions:

Conceptualization: Kunal Chakraborty
Data curation: A. P. Joshi, Prasanna Kanti Ghoshal, Balaji Baduru, Vinu Valsala, V. V. S. S. Sarma, Nicolas Metzl, Marion Gehlen, Frédéric Chevallier, Claire Lo Monaco
Formal analysis: Kunal Chakraborty, A. P. Joshi, Vinu Valsala
Investigation: A. P. Joshi, Prasanna Kanti Ghoshal, Balaji Baduru
Methodology: Kunal Chakraborty
Resources: Kunal Chakraborty
Software: A. P. Joshi, Prasanna Kanti Ghoshal, Balaji Baduru
Validation: A. P. Joshi, Prasanna Kanti Ghoshal, Balaji Baduru
Visualization: Kunal Chakraborty, Vinu Valsala, V. V. S. S. Sarma, Nicolas Metzl
Writing – original draft: Kunal Chakraborty
Writing – review & editing: Vinu Valsala, V. V. S. S. Sarma,

Indian Ocean Acidification and Its Driving Mechanisms Over the Last Four Decades (1980–2019)

Kunal Chakraborty[1] , A. P. Joshi[1] , Prasanna Kanti Ghoshal[1,2] , Balaji Baduru[1,3] , Vinu Valsala[3] , V. V. S. S. Sarma[4] , Nicolas Metzl[5] , Marion Gehlen[6] , Frédéric Chevallier[6] , and Claire Lo Monaco[5]

[1]Indian National Center for Ocean Information Services, Ministry of Earth Sciences, Hyderabad, India, [2]Faculty of Ocean Science and Technology, Kerala University of Fisheries and Ocean Studies, Kochi, India, [3]Indian Institute of Tropical Meteorology, Ministry of Earth Sciences, Pune, India, [4]CSIR-National Institute of Oceanography, Regional Center, Visakhapatnam, India, [5]Laboratoire LOCEAN/IPSL, Sorbonne Université-CNRS-IRD-MNHN, Paris, France, [6]Laboratoire des Sciences du Climat et de l'Environnement, LSCE-IPSL, CEA-CNRS-UVSQ, Université Paris-Saclay, Gif-sur-Yvette, France

Abstract This paper aims to study the changes in the Indian Ocean seawater pH in response to the changes in sea-surface temperature, sea-surface salinity, dissolved inorganic carbon (DIC), and total alkalinity (ALK) over the period 1980–2019 and its driving mechanisms using a high-resolution regional model outputs. The analysis indicates that the rate of change of declining pH in the Arabian Sea (AS), the Bay of Bengal (BoB), and the Equatorial Indian Ocean (EIO) is −0.014 ± 0.002, −0.014 ± 0.001, and −0.015 ± 0.001 unit dec^{-1}, respectively. Both in AS and BoB (EIO), the highest (lowest) decadal DIC trend is found during 2000–2009. The surface acidification rate has accelerated throughout the IO region during 2010–2019 compared to the previous decades. Further, our analysis indicates that El Niño and positive Indian Ocean Dipole events lead to an enhancement of the Indian Ocean acidification. The increasing anthropogenic CO$_2$ uptake by the ocean dominantly controls 80% (94.5% and 85.7%) of the net pH trend (1980–2019) in AS (BoB and EIO), whereas ocean warming controls 14.4% (13.4% and 7.0%) of pH trends in AS (BoB and EIO). The changes in ALK contribute to enhancing the pH trend of AS by 5.0%. ALK dominates after DIC in the EIO and, similar to the AS, contributes to increasing the negative pH trend by 10.7%. In contrast, it has a buffering effect in the BoB, suppressing the pH trend by −5.4%.

Plain Language Summary The oceans play a significant role in regulating the amount of CO$_2$ in the atmosphere. The increasing oceanic uptake of CO$_2$ counterbalances the increase in atmospheric CO$_2$. This uptake has a considerable impact on marine biogeochemistry, leading to pH and alkalinity imbalances in the water column, commonly referred to as ocean acidification. In an acidic ocean, excess CO$_2$ reacts with seawater to form carbonic acid, which is highly unstable and undergoes further reduction by releasing hydrogen ions (H$^+$) and acidifying the seawater (reduces the pH). Several studies have projected a decline of upper ocean pH by 0.3–0.4 by the end of the 21st century, which has the potential to reduce oceanic biological production considerably. The number of available observations to study Indian Ocean acidification is limited. There is a critical need to understand the status of Indian Ocean acidification and identify its key drivers. This article consolidates the current level of understanding about the Indian Ocean acidification based on the available field observations, reconstructed data sets, and model simulations.

1. Introduction

Anthropogenic activities like deforestation, land-use land-cover change, cement production, and fossil fuel emission since the industrial revolution have been increasing the levels of atmospheric CO$_2$ (Friedlingstein et al., 2022; Le Quéré, Andrew, Friedlingstein, Sitch, Hauck, et al., 2018; Le Quéré, Andrew, Friedlingstein, Sitch, Pongratz, et al., 2018). The growth rate of atmospheric CO$_2$ has increased to ≈5.7 ± 0.1 PgC yr^{-1} in 2021 from ≈1.7 ± 0.1 PgC yr^{-1} in the 1960s (Friedlingstein et al., 2022). Nearly half of this anthropogenically emitted CO$_2$ is absorbed by land and ocean together (Canadell et al., 2021). According to the Global Carbon Budget, 2022, the ocean absorbed ≈28% of the total CO$_2$ emissions in 2021 (Friedlingstein et al., 2022).

The increasing oceanic uptake of CO$_2$ has a considerable impact on marine ecosystems as it causes pH reduction in the water column, which is commonly referred to as ocean acidification. There has been growing concern for

Nicolas Metzl, Marion Gehlen,
Frédéric Chevallier, Claire Lo Monaco

the potential adverse impacts of slowly acidifying the Indian Ocean (IO). Dalpadado et al. (2023) reported significant effects of the IO acidification on coral reefs and shell-forming living organisms (like gastropods, bivalves, and many more). The IO basin is geographically smaller than the Pacific and Atlantic, whereas the land enclosing the north makes it a geographically unique basin. The coasts of the IO accommodate approximately 30% of the world's population (Wafar et al., 2011), resulting in higher anthropogenic activities. The north IO receives high freshwater flux from local precipitation and high discharge from perennial rivers (such as Ganga and Brahmaputra) (UNESCO, 1969). The seasonal reversing winds in the northern IO result in seasonal reversing currents (Shetye et al., 1996). This seasonal reversal of currents substantially controls the carbon and nitrogen cycles of the IO (Chakraborty et al., 2021; Joshi et al., 2021; Sarma et al., 2018; Sreeush et al., 2018).

The carbonate chemistry of the regional IO is comparatively poorly studied than to the Pacific and Atlantic, especially in terms of long-term analysis. The paucity of observational data is a major obstacle and the main reason this region is understudied. However, appreciable efforts are being made to explore the carbonate dynamics of this region (Chakraborty et al., 2021; Ghosh et al., 2021; Joshi & Warrior, 2022; Sreeush et al., 2020; Valsala et al., 2012; Valsala & Maksyutov, 2013). It is shown that both physical (upwelling, seasonal reversal of currents, mixing, etc.) and biological (such as photosynthetic uptake of CO_2, respiration, remineralization, etc.) processes primarily control the spatial and temporal variability of surface pCO_2 (partial pressure of CO_2) and associated sea-to-air CO_2 flux (Chakraborty et al., 2018; Valsala et al., 2020; Valsala & Maksyutov, 2013). The modeling studies in the Arabian Sea (AS) and Bay of Bengal (BoB) show that temperature and DIC are the primary drivers controlling the seasonality of pCO_2 (Chakraborty et al., 2021; Joshi et al., 2020). The climate indices like the Indian Ocean Dipole (IOD) and El Ninõ southern oscillations (ENSO) also play an important role in regulating the interannual variabilities of the sea-air CO_2 flux, especially in the subtropical IO and the western AS (Valsala et al., 2020; Valsala & Maksyutov, 2013). Valsala et al. (2020) reported that the sea-to-air CO_2 fluxes, pCO_2, DIC and ALK vary by as much as ± 1 mol m^{-2} yr^{-1}, ± 20 μatm, ± 35 μmole kg^{-1} and ± 22 μmole kg^{-1} within 80–105°E, 0–10°S due to IOD, respectively.

Despite the rise in the atmospheric CO_2, the north IO (north of 35°S) is known to be a moderate sink of the atmospheric CO_2 (Chau et al., 2022; Sarma et al., 2013, 2023; Takahashi et al., 2009; Valsala & Maksyutov, 2010). Sea-to-air fluxes of CO_2 are known to be maximum during the summer monsoon season in the AS (De Verneil et al., 2022; Sreeush et al., 2018). The BoB carbon cycle (which affects the CO_2 source and sink characterstics of this region) is strongly regulated by high river discharge and local precipitation (Chakraborty et al., 2021; Joshi et al., 2021, 2022; Joshi & Warrior, 2022; Kumar et al., 1996; Sridevi & Sarma, 2021). The peninsular rivers of BoB bring acidic and pCO_2-rich waters to the ocean; hence, the south-western BoB acts as a source of atmospheric CO_2 (Joshi et al., 2021; Sarma et al., 2012). On the contrary, glacial rivers, such as Ganges and Brahmaputra, bring basic and pCO_2-poor waters to the coast, which makes the northern BoB a sink of atmospheric CO_2 (Joshi et al., 2021; Sarma et al., 2012). Therefore, the impact of river discharge is not uniform in the BoB. Moreover, the aerosol deposition and increase in river discharge due to global warming influence the interannual variability of surface pCO_2, CO_2 flux, and pH in the BoB (Sridevi & Sarma, 2021). The uncertainties associated with the CO_2 flux are shown to be higher in the numerical models (≈ 0.1 to 0.12 PgC yr^{-1}) than observations-based models (≈ 0.002 to 0.03 PgC yr^{-1}) (Chau et al., 2022). The limited number of observations in the north Indian Ocean increases the uncertainty in estimating surface pCO_2 and associated air-sea CO_2 flux (Chau et al., 2022, 2024).

The storage of anthropogenic CO_2 (C_{ant}) in the Indian Ocean was first estimated from observation data collected during the World Ocean Circulation Experiment (Sabine et al., 1999) and its decadal changes evaluated using data incorporated in GLODAP (Gruber et al., 2019; Müller et al., 2023). These studies indicate an increase of C_{ant} in the water column which may affect the Indian Ocean acidification. For the period 1991–2011, Lauvset et al. (2015) reported a decreasing rate for the IO surface pH by -0.027 ± 0.005 dec^{-1} using the available observations from the Surface Ocean CO_2 Atlas (SOCAT)v2. In a recent study, Chau et al. (2024) reported a lower rate of decrease of the IO pH by -0.017 ± 0.001 dec^{-1} for the period 1985–2019. Interestingly, in another study, Ma et al. (2023) estimated a further lower rate of decrease in the IO surface pH for the period 1982–2021 (-0.0155 ± 0.0009 dec^{-1}) compared to Lauvset et al. (2015). An observations-based regional study in the Mozambique region showed an increase in the pH declining trend in recent decades (Lo Monaco et al., 2021). Therefore, it is clear that there is a considerable difference in the Indian Ocean acidification rate estimates derived using different approaches for different periods.

Sarma et al. ([2023](#)) demonstrated that the spatial and temporal variability of CO_2 fluxes is better captured by regional than global models. The errors in the reconstruction of pH among the global products are globally not uniform. We must acknowledge the errors in observations-based global products due to mapping methods, particularly in higher latitudes (Burger & Frölicher, [2023](#)). Specifically, this difference is most appreciable where sufficient observations are unavailable, such as in the Indian Ocean. On the other hand, high-resolution regional models have shown notable skill in simulating mesoscale processes and capturing coastal processes. This creates the opportunity, and perhaps necessity, to develop numerical solution schemes that adapt the resolution in specific areas of interest. Hence, this study attempts to understand long-term changes in the carbon cycle for the IO region using a high-resolution regional model outputs and its comparison with synthesized data products and outputs from a global model simulation. We ran a regional, high-resolution coupled ocean-ecosystem model for 40 years and evaluated the trend of acidification and driving mechanisms controlling the trend. We hypothesize that this analysis will provide a deeper understanding of the factors regulating the evolution of carbonate chemistry for the entire IO region.

2. Data and Methodology

This section comprehensively describes the configuration of a high-resolution regional model, which is used for a plausible reconstruction of the physics and carbonate chemistry of the IO when forced by reanalysis. Besides this, an offline global biogeochemical model simulated outputs are also used for analysis. Along with the in-situ observations, this study uses two global machine learning-based products (OceanSODA-ETHZv2023 (Ocean-SODA) (Gregor & Gruber, [2021](#); Ma et al., [2023](#)) and Copernicus Marine Environment Monitoring Service Laboratoire des Sciences du Climat et de l'Environnement feed-forward neural network (CMEMS-LSCE-FFNN (Chau et al., [2024](#))) for analysis. The cluster and training for each cluster method (GRaCER) used for preparing OceanSODA should emulate suitable regional ocean acidification. CMEMS-LSCE-FFNN is the latest machine learning-based study with a higher resolution than OceanSODA, which should be an advantage in regional acidification studies (expected to be a better product for the near coastal and coastal regions). Owing to these advantages in machine learning-based products, we use OceanSODA and CMEMS-LSCE-FFNN to compare our regional model results. Further details of the methodology, in-situ observations and machine learning products are provided hereafter in this section.

2.1. Models

2.1.1. INCOIS-BIO-ROMS Modeling System

Biogeochemical State of the Indian Ocean (BIO) is a high-resolution, coupled ocean-ecosystem modeling system developed at the Indian National Center for Ocean Information Services (INCOIS) under the modeling projects of the Ministry of Earth Sciences (MoES), which integrates ocean simulation, observation, and analysis to study the role ocean physics plays in marine environmental health and ecosystem functioning in the coastal ocean and adjacent deep sea. The modeling framework involves an online coupling of the Ocean General Circulation Model dynamics integrated with an ecosystem model at scales that resolve the variability of the region's physics and ecosystems.

Further, the international carbon cycle research community carried out the largest, most comprehensive assessment to better quantify and understand the CO_2 fluxes into and out of the ocean, the associated changes in ocean carbon storage beneath the sea surface, as well as the role of the ocean's biological pump in the form of "REgional Carbon Cycle Assessment and Processes Phase 2 (RECCAP-2)" to assist IPCC. To participate in the RECCAP-2 assessment process, a regional high-resolution (1/12°) coupled ocean-ecosystem model (INCOIS-BIO-ROMS) for the Indian Ocean region was configured as a part of the BIO modeling system following the "RECCAP-2: Ocean Modeling Protocol" for the regional Oceans.

The ocean general circulation model used for simulating the ocean carbon cycle variability of the Indian Ocean is the Regional Ocean Modeling System (ROMS; version 3.9). The scientific community widely uses ROMS, a free-surface, terrain-following, primitive equations ocean model, for a diverse range of applications. The physical model is coupled to an ecosystem model (Fennel et al., [2006](#), [2008](#), [2013](#); Laurent et al., [2017](#)). The model has a horizontal grid resolution of 1/12° (approximately 9 km) and uses 40 vertical layers in a terrain-following

coordinate system. A ROMS-based coupled, high-resolution ocean-ecosystem modeling system, known as INCOIS-BIO-ROMS, has been developed for the Indian Ocean basin. For more details, please refer to Chakraborty et al. (2017, 2018, 2019, 2021).

The model state of the carbon state variables has been initialized using quality-controlled observation from the Global Ocean Data Analysis Product (GLODAPv2 (Key et al., 2004; Lauvset et al., 2021)). The model is initialized for the early 1970s, followed by the spin-up phase for the 1970s, during which atmospheric CO_2 rises according to the observations. The atmospheric history of the pCO_2 has been taken from Keeling et al. (1995) at monthly resolutions. From 1980 onward, the simulation continued until 2019, providing the basis for the analyses.

An ensemble coupled data assimilation (ECDA) system simulated reanalysis data produced by the Geophysical Fluid Dynamics Laboratory has been used to prescribe open boundaries for the INCOIS-BIO-ROMS. The reanalysis data have a zonal resolution of 1° with 360 grid points longitudinally and 1° at higher latitudes but have a finer resolution of 0.8° in the tropics, with 200 grid points along the latitude. The data have 50 vertical levels with 10 m increments in the upper 225 m and stretched vertical levels after 225 m depth. The horizontal grids are in spherical coordinates, and the vertical grids are in z levels. The data are available as monthly means centered on the 15th of every month from 1960 to 2019 (Chang et al., 2013).

The model has been forced by observed climate (e.g., from reanalysis products) and observed atmospheric CO_2 throughout the entire simulation time to reproduce the interannual variability and trend in the ocean carbon uptake in response to changes in both atmospheric CO_2 and climate during the model simulation period from 1980 to 2019. To ensure continuity in forcing, that is, only one forcing data for the entire time series of the analysis period, that is, 1980 through 2019, the reanalysis product Japanese 55-year Reanalysis-Driving Ocean (JRA55-do) has been used (Tsujino et al., 2018).

The monthly river discharge has been implemented as a freshwater flux from the JRA55-do forcing data set (Tsujino et al., 2018). The JRA55-do data set includes the daily river runoff produced by a global river hydrodynamic model forced by an adjusted runoff from the land-surface component of the Japanese 55-year Reanalysis (JRA-55) (Suzuki et al., 2018). The transport of associated concentrations of tracers (temperature, salt, nutrients, carbon fluxes, etc.) from rivers into the ocean has been prescribed using available observations. The point-source method is used to distribute the freshwater discharge volume of all the rivers individually in the model grids. The river's total volume flux distribution occurs in single or multiple horizontal grid points identified at the river drainage points and the corresponding vertical levels. The freshwater gets spread throughout the domain following the ocean general circulation.

2.1.2. OTTM Biogeochemistry and Carbon Cycle Model

Ocean Tracer Transport Model (OTTM) simulates the global ocean biogeochemistry and carbon cycle (Valsala et al., 2008; Valsala & Maksyutov, 2010). It is an offline model driven by a re-analyzing ocean currents and other data from the ECDA system (Chang et al., 2013). Ocean Tracer Transport Model utilizes a phosphate restoration approach to calculate the biological pumps and OCMIP-2 protocols to solve the surface ocean carbonate chemistry. A spatio-temporal community compensation depth is parameterized to reduce the biases in the seasonal cycle of pCO_2 (Sreeush et al., 2018, 2020). The details of the model simulations can be found at Valsala et al. (2020). The model outputs from 1980 to 2019 are used in this study.

2.2. Data

We use time series observations of pCO_2 and pH from a mooring and ship-based observations of pCO_2 available from SOCATv2022 database to validate both the regional and global model simulated outputs. Further, the long-term evolution of various state variables from the model is compared to corresponding estimates from observations-based Machine-Learning (ML) models. Thus, the analysis presented in this paper has been carried out using the outputs from a high-resolution regional ocean-ecosystem model (ROMS Chakraborty et al., 2017, 2018, 2019, 2021) and a global biogeochemistry model (OTTM (Valsala et al., 2008; Valsala & Maksyutov, 2010)) along with reconstructed data sets from two state-of-the-art global data products of the surface ocean CO_2 system, CMEMS-LSCE-FFNN (Chau et al., 2024) and OCEAN-SODA (Gregor & Gruber, 2021). The
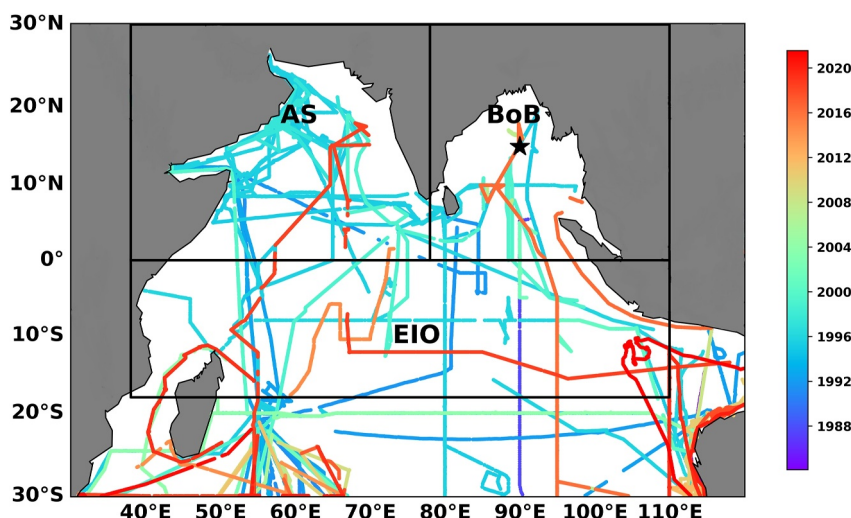
Figure 1. Representation of SOCATv2022 (1980–2022) cruise lines (color represents the year of cruise occurrence), BOBOA mooring (Black star), and three regions of analysis. The AS stands for the Arabian Sea, BoB for the Bay of Bengal, and the Equatorial Indian Ocean.

details of the data used in this study are described below. Figure 1 depicts the available in-situ measurements from different cruises and mooring-based measurements used in this study.

2.2.1. BOBOA Mooring

In the IO, the consistent and long-term surface pCO_2 and pH data is available only from a RAMA buoy located at 15°N, 90°E in the BoB, commonly known as the BoB Ocean Acidification (BOBOA) moored buoy (Sutton et al., 2014, 2019). The Research Moored Array for African-Asian-Australian Monsoon Analysis and Prediction (RAMA) network includes this mooring. The frequent cyclones in BoB and the maintenance activities make it challenging to have continuous measurements from this mooring. Table 1 indicates that the buoy has four active periods. The wind speed, currents, precipitation, and density measurements are also available from this buoy in addition to the variables listed in Table 1.

2.2.2. SOCAT Data

The Surface Ocean CO_2 Atlas (SOCATv2022; Bakker et al. (2016, 2022)) is a publicly available in-situ database for quality-controlled surface fCO_2 (the fugacity of the CO_2) observations. SOCAT version 2022 has quality-controlled in-situ surface ocean fCO_2 measurements made on ships, moorings, autonomous, and drifting surface platforms for the global ocean and coastal seas from 1957 to 2021. The SOCAT synthesis and gridded products contain 33.7 million fCO_2 values with an estimated accuracy of <5 μatm. To keep consistency with model outputs, we convert fCO_2 to pCO_2 using the MATLAB CO2SYS program (Van Heuven et al., 2011).

2.2.3. OceanSODA Data

The OceanSODA is an observations-based gridded ($1° \times 1°$) product, which provides carbonate variables from 1982 through 2021 (Gregor & Gruber, 2021). The product extrapolates in space and time surface pCO_2 from SOCAT and ALK from GLODAP using GRaCER (Geo-spatial Random Cluster Ensemble Regression) method. The GRaCER method creates spatial clusters and applies machine learning algorithms (Neural Network and Gradient Boosting) on each cluster. Using thermodynamic equations, other carbonate variables (such as DIC, Aragonite, and pH) are computed based on the pCO_2 and ALK.

Table 1
BOBOA Mooring Data Details (Adopted From Sutton et al. (2019), Joshi et al. (2020, 2021))

Location	15°N 90°E
Type	Time series data
Temporal Resolution	3 hourly data (converted to daily for this study)
Duration	24 Nov 2013 to 6 Dec 2014 (Deployment 1)
	6 Dec 2014 to 19 Jun 2015 (Deployment 2)
	6 Mar 2016 to 9 Jan 2017 (Deployment 3)
	11 Jan 2017 to 20 Nov 2018 (Deployment 4)
Variables	Seawater pCO_2, pH, SST, SSS
Investigator Institution	Pacific Marine Environmental Laboratory

2.2.4. CMEMS-LSCE-FFNN Data

The CMEMS-LSCE-FFNN is developed using an ensemble-based approach described in Chau et al. (2022). For this study, the latest version (Chau et al., 2024) is used consisting of monthly reconstructed surface pCO_2 and CO_2 fluxes at a spatial resolution of $0.25° \times 0.25°$ over the global and coastal oceans. Carbonate variables are computed at the same spatial and temporal resolution using the CO2SYS software (Lewis et al., 1998; Van Heuven et al., 2011) with the reconstructions of pCO_2 and ALK, as well as nutrient concentrations (silicate, phosphate), physical variables (sea-surface temperature (SST) and sea-surface salinity (SSS)), and dissociation constants as inputs. Chau et al. (2022, 2024) provide details of the algorithms and derivations. ALK is derived from Local Interpolated Alkalinity Regression (Carter et al., 2018).

2.3. Methods

2.3.1. Statistics for Model Evaluation

This section describes different statistics employed in this study. The first is the correlation coefficient (r), which explains how well the model reproduces observations. The root mean square error (RMSE) provides insight into the closeness between the model and observed values. The central tendency measures (mean, median, and mode) compare the model's and observation's statistical distribution. Along with central tendencies, spread measures such as standard deviation (STD), Inter Quartile Range, Skewness, and Kurtosis are used to gain perspective on the total spread of model simulations and observations.

2.3.2. Drivers

The changes in DIC, ALK, SST, and SSS primarily govern the spatial and temporal variability of pH and pCO_2. The effect of each of these drivers has been analyzed using a decomposition analysis (Takahashi et al., 1993; J. L. Sarmiento, 2013; Takahashi et al., 2014; Chakraborty et al., 2021; Joshi & Warrior, 2022). The equation can be expressed based on Taylor series expansion as follows.

$$\frac{dX}{dt} = \frac{\partial X}{\partial DIC}\frac{dDIC}{dt} + \frac{\partial X}{\partial ALK}\frac{dALK}{dt} + \frac{\partial X}{\partial SST}\frac{dSST}{dt} + \frac{\partial X}{\partial SSS}\frac{dSSS}{dt} + (other\_minor\_ions) \qquad (1)$$

where X represents either pH or pCO_2.

The left-hand side of Equation 1 shows the temporal variation of pCO_2 or pH. The right side of Equation 1 represents the changes in X due to the changes in each of the drivers. The reconstructed pCO_2 and pH is denoted as CTRL. We use the abiotic pump routines of OCMIP-2 to reconstruct the pCO_2 and pH using model-simulated DIC, SST, SSS, and ALK. To assess the sensitivity of each of these drivers, we reconstruct the pCO_2 or pH separately for each driver by providing the detrended values of the corresponding driver while keeping the other drivers as it is. If the SST is our driver for which we want to assess the sensitivity, then we denote it as SEN(SST). Now, subtracting the sensitivities (such as SEN(SST)) separately for each of the drivers from the CTRL provides the required quantification of each of these drivers in the trend of pCO_2 and pH.

2.3.3. Empirical Orthogonal Function (EOF) Analysis

In climate studies, Empirical Orthogonal Function (EOF) analysis is often used to identify plausible temporal changes in the variability of spatial patterns. We perform an EOF analysis to understand the effect of interannual climate signals like ENSO and IOD on ocean acidification in IO. The long-term simulation of ROMS for a prolonged duration (40 years) resolves the interdecadal variability and long-term trends along with interannual variability of the carbonate variables (Valsala et al., 2020). We carried out an EOF analysis to analyze the interannual variability of pH (pCO_2). Before the EOF analysis, we remove a 5-year running climatology from ROMS simulated pH (pCO_2) and normalize these anomalies using the STD for the same 5-year period following the procedure described in Valsala et al. (2020). To understand the effect of ENSO and IOD, we correlate the principal components (PC) with the Nino3.4 and Dipole Mode Index (DMI) indices. The Nino3.4 indices are the SST anomaly difference in the central equatorial Pacific region, which is an indicator of the ENSO events. The DMI is defined as the difference in SST anomaly between the western part of the IO and the eastern part of the IO, which is an indicator of the IOD events.
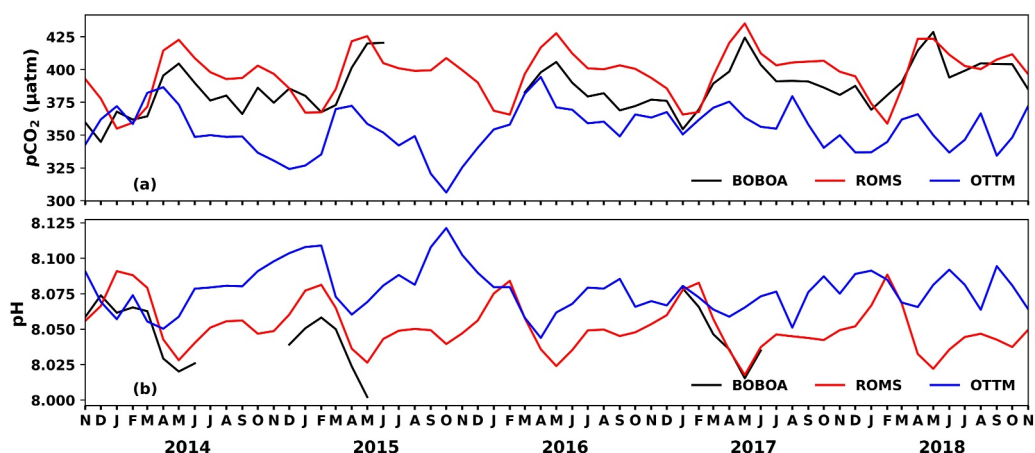
Figure 2. Figure (a) shows the time-series comparison of model simulated outputs (red line indicates ROMS and blue line indicates OTTM) with BOBOA (black line) mooring observations for $p\mathrm{CO_2}$. Figure (b) is the same as (a) but for pH.

3. Results and Discussions

3.1. Model Evaluation

We compare ROMS and OTTM simulated outputs against available SOCAT observations and the measurements available from the BOBOA mooring to evaluate the capability of models in resolving spatio-temporal variability of $p\mathrm{CO_2}$ and pH. Since SOCAT does not include pH data, a comparison of ROMS and OTTM simulated outputs against the most recent observations-based reconstructed data products (CMEMS-LSCE-FFNN and Ocean-SODA) is also presented here to check the capability of an eddy-resolving (eddy-permitting) regional (global) model in reproducing the Indian Ocean carbon cycle.

3.1.1. Evaluation With the BOBOA Mooring Data

The surface $p\mathrm{CO_2}$ observations are available from the BOBOA mooring from November 2013 till November 2018 (please see Section 2.2.1). We extract the model simulated (ROMS and OTTM) time series for a similar period for the mooring location (using nearest neighbor interpolation) to make a comparison. From Figures 2a and 2b, we observe that the ROMS captured the seasonal cycle of $p\mathrm{CO_2}$ and pH better than OTTM. Compared with mooring data, the ROMS leads the peaks and troughs. The correlation between the ROMS (OTTM) and BOBOA for $p\mathrm{CO_2}$ is 0.79 (0.19), and for pH, it is 0.88 (0.38). The correlation shows that ROMS can capture the seasonality adequately. The lowering of surface $p\mathrm{CO_2}$ due to the freshwater impact from rivers and precipitation is well emulated by ROMS. The October-November months are known to have the lowest surface $p\mathrm{CO_2}$ due to the maximum spread of the freshwater plume (Joshi et al., 2021), this too is well captured by ROMS. Sea-surface temperature is known to drive the increase in surface $p\mathrm{CO_2}$ from Jan to Sep (Chakraborty et al., 2021; Joshi & Warrior, 2022), which is also well captured by ROMS. The seasonality of pH is opposite to that of $p\mathrm{CO_2}$, which shows high pH in months of freshwater dominance (refer Figure 2b). The ROMS model overestimates both $p\mathrm{CO_2}$ (RMSE of 16.6 μatm and mean bias of 11.21 μatm) and pH (RMSE of 0.016 and mean bias of 0.01 units) while the OTTM model underestimates $p\mathrm{CO_2}$ (RMSE of 36.44 μatm and mean bias of -29.13 μatm) and overestimates pH (RMSE of 0.035 and mean bias of 0.03 units), as observed from Figure 2. These discrepancies could be attributed to the biases in model simulated physical and biogeochemical states. Further, the limited number of pH observations from the BOBOA mooring is a constraint in validating modeled pH in the IO region. The mooring represents a single location, whereas the corresponding model values are sampled from a grid encompassing the mooring location, and some of the discrepancies in the comparison may arise from this fact. Nevertheless, the comparison of the seasonal cycle of $p\mathrm{CO_2}$ and pH is encouraging.

3.1.2. Evaluation With SOCAT Data

The SST, SSS, and $p\mathrm{CO_2}$ observations available from the SOCAT database have been utilized to establish the capability of ROMS ($p\mathrm{CO_2}$ from OTTM) model in simulating spatial variability of these variables. The ROMS
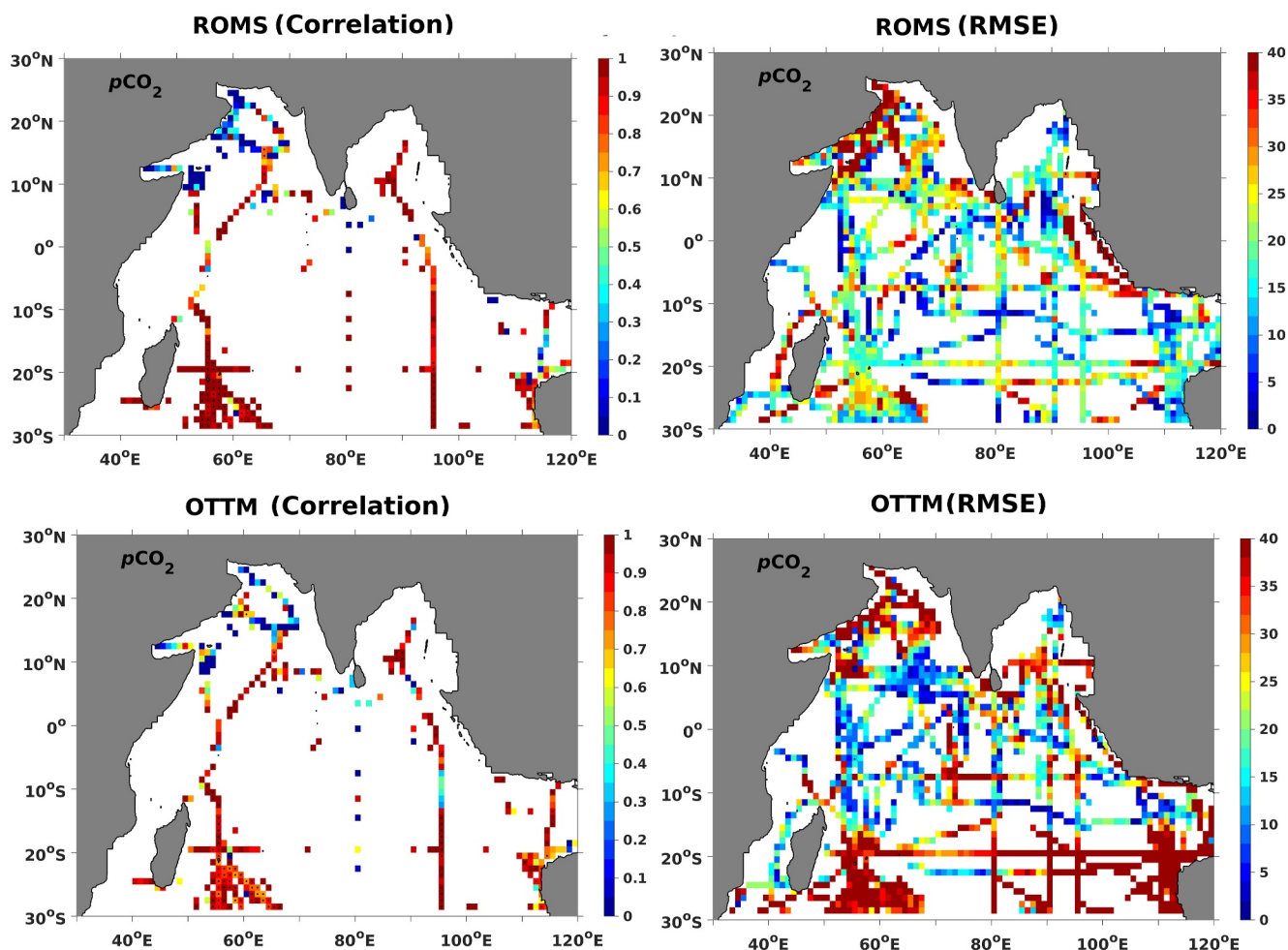
Figure 3. Correlation and RMSE of ROMS and OTTM simulated outputs with the available SOCAT grided data (1° × 1°). Simulated pCO_2 (ROMS in first row and OTTM in second row) comparison with SOCAT observations. The black dot in shaded spatial correlation indicates the locations with more than 95% significant correlation.

simulated estimates of SST, SSS, and pCO_2 as well as OTTM simulated pCO_2, are compared with SOCAT track data from 1980 to 2019. Model estimates are projected on the time-space of SOCAT monthly track data adding up to approximately 3,100 observations over the IO region from 1980 to 2019. Spatial RMSE is computed at all the available grid points with at least one observation. Spatial correlation is computed for only those grid points with at least three observations and is shaded with respective correlations ranging between 0 and 1. The spatial distribution of the p-value and number of available observations at each grid point are provided in Figure S1 in Supporting Information S1.

To understand the spatial agreements between ROMS (OTTM) outputs and SOCAT observations, we plot spatial correlation and RMSE in Figure 3 (Figure S2 in Supporting Information S1). The mean correlation coefficient between ROMS simulated SST, SSS, pCO_2, and SOCAT observations are, respectively, 0.94, 0.80, and 0.63 (0.44 for OTTM simulated pCO_2) (with 95% confidence level). Similarly, the mean RMSE for SST, SSS, and pCO_2 are 0.89°C, 0.64, and 30.02 (37.65 for OTTM simulated pCO_2) µatm. The statistical analysis indicates that ROMS captures the observed variability of pCO_2 in the IO (30°S to 30°N and 30°E to 120°E) better than OTTM. Slightly high values of RMSE in both models could be due to the temporal discontinuity of the SOCAT observations. ROMS simulated SST and SSS have been observed to correlate well with low RMSE values throughout the IO except for a few points in the AS when compared with the SOCAT based observations (Figure S2 in Supporting Information S1). Further details are provided in the supplementary document. The pCO_2 comparison between the models (ROMS and OTTM) and SOCAT in the first and second rows of Figure 3 reveals
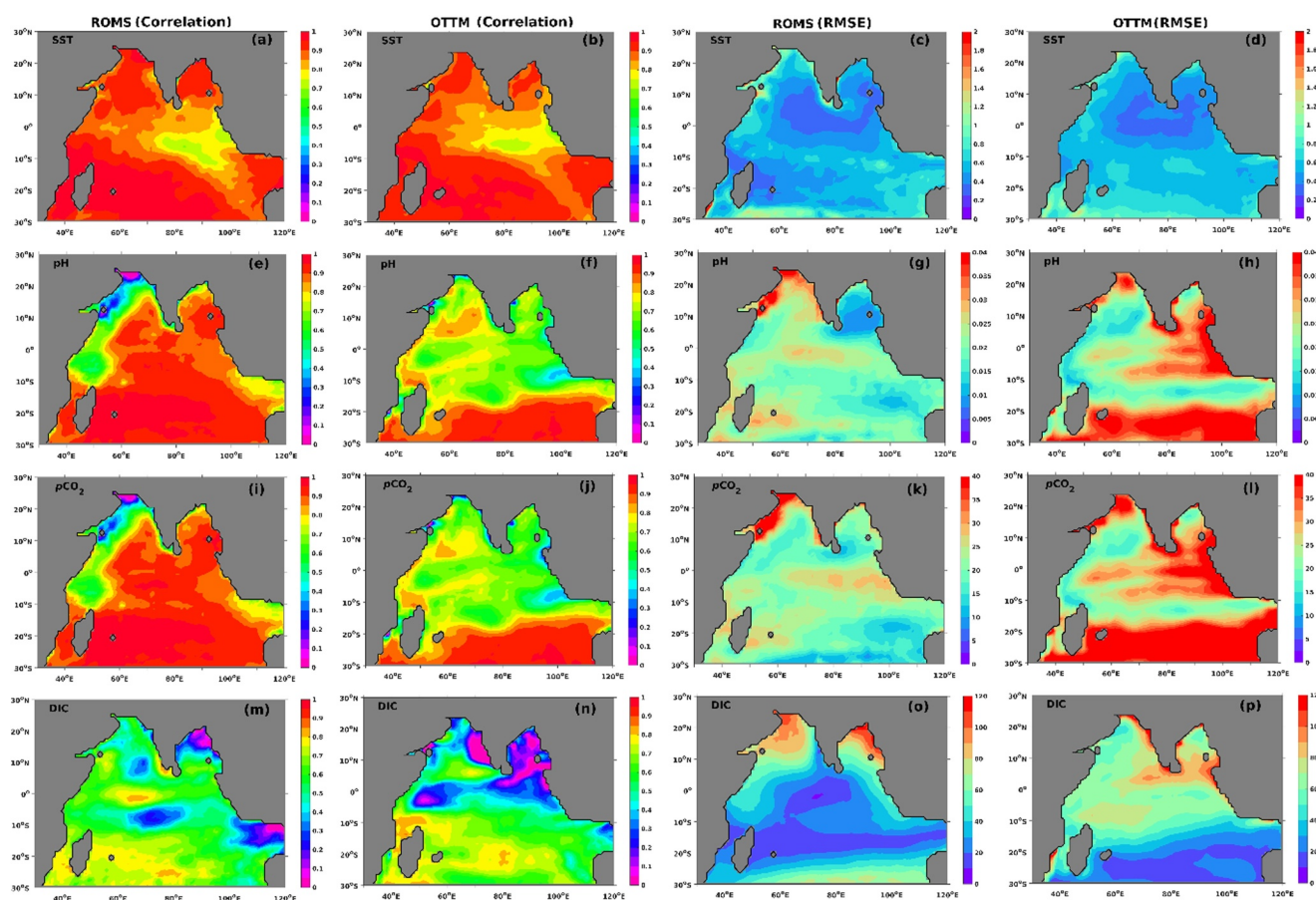
Figure 4. In the first panel, figures (a–d) represent the correlation and RMSE between ROMS and OTTM simulated SST and the reconstructed SST from OceanSODA. In the second panel, figures (e–h) represent the correlation and RMSE between ROMS and OTTM simulated surface pH and the reconstructed pH from OceanSODA. In the third panel, figures (i–l) show the correlation and RMSE between ROMS and OTTM simulated pCO_2 and the reconstructed pCO_2 from OceanSODA, and in the fourth panel, figures (m–p) represent the same statistics but between ROMS and OTTM simulated DIC and the reconstructed DIC from OceanSODA.

high RMSE and low correlation in the northwestern coast of the AS. The OTTM model shows high RMSE in the south, that is, below 20°S likely due to the overestimation of biological pumps (Valsala et al., 2020). OTTM's RMSE within the region of ±20°S is smaller than in the subtropics. The higher RMSE in the coastal upwelling zone (northwestern AS) could be due to a stronger upwelling simulated by the models. The stronger upwelling may result from the high spatial model resolution (for ROMS) and the use of the KPP vertical mixing scheme, known to enhance vertical mixing (Chakraborty et al., 2019).

3.1.3. Consistency With OceanSODA Data

The consistency between ROMS, OTTM, and OceanSODA data is shown in Figure 4. The correlation between modeled (ROMS and OTTM) SST and OceanSODA SST is above 0.8 throughout the IO domain, except for the central-eastern region (Figures 4a and 4b). The spatial RMSE in SST is below 1–1.2°C throughout the IO domain (Figures 4c and 4d). The northwestern region (especially near the coast) is observed to have higher RMSE. The IO domain average temporal comparison between ROMS (OTTM) and OceanSODA reveals the mean correlation to be 0.97 (0.98) (95% significance) and the mean RMSE to be 0.62 (0.56) °C. Here it is to be noted that OTTM is an offline biogeochemistry model driven by the physical state variables from a reanalysis product.

Figures 4e, 4f, 4i, and 4j represent the correlation of pH (pCO_2) between models (ROMS and OTTM) and OceanSODA, respectively. The spatial pH in ROMS correlates better than pH in OTTM when compared with OceanSODA (Figures 4e, 4f, 4i, and 4j). Low correlation (0.6–0.7) for ROMS of pH and pCO_2 are evident only in the northwestern region (could be due to the bias in estimating upwelling strength). In contrast, a high correlation
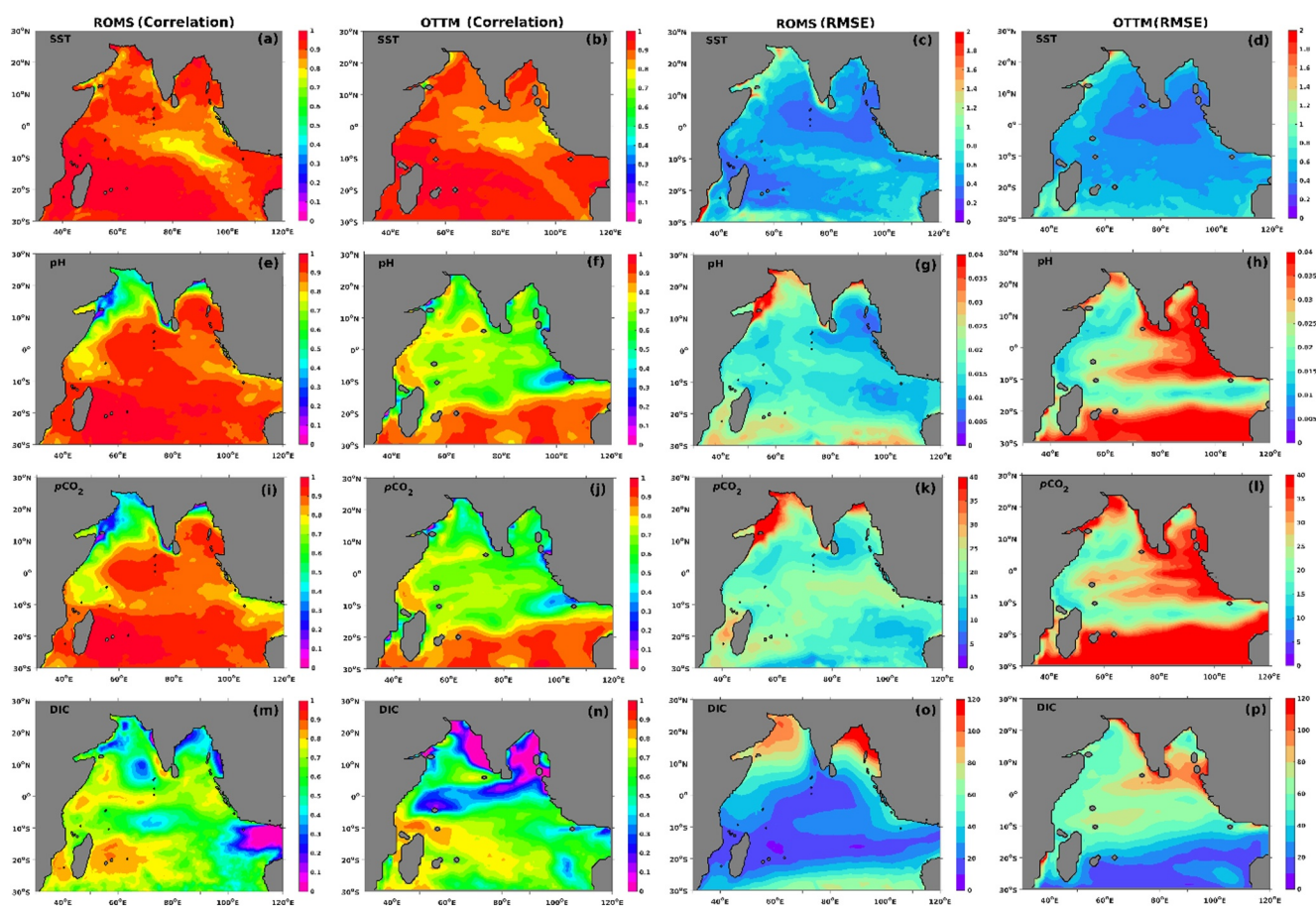
Figure 5. In the first panel, figures (a–d) represent the correlation and RMSE between ROMS and OTTM simulated SST and the reconstructed SST from CMEMS-LSCE-FFNN. In the second, figures (e–h) represent the correlation and RMSE between ROMS and OTTM simulated surface pH and the reconstructed pH from CMEMS-LSCE-FFNN. In the third panel, figures (i–l) show the correlation and RMSE between ROMS and OTTM simulated pCO_2 and the reconstructed pCO_2 from CMEMS-LSCE-FFNN, and in the fourth panel, figures (m–p) represent the same statistics but between ROMS and OTTM simulated DIC and the reconstructed DIC from CMEMS-LSCE-FFNN.

(above 0.8) is seen in the rest of the IO domain. The RMSE in the OTTM model is higher with respect to ROMS for both pH (Figures 4g and 4h) and pCO_2 (Figures 4k and 4l). Figures 4g and S3l in Supporting Information S1 show high RMSE values for the OTTM model in the region below 20°S and the eastern domain above 10°S for both pCO_2 (above 35 μatm) and pH (above 0.035). The RMSE in ROMS is high only in the northwestern zone (Figures 4g and S3k in Supporting Information S1). The domain average correlation between ROMS (OTTM) and OceanSODA for pH (0.84 (0.49)) and pCO_2 (0.82 (0.50)) shows that ROMS can satisfactorily capture the temporal variability of both variables. However, here we must note that OceanSODA is an extrapolated data product developed using the available observations of pCO_2 and ALK, and the rest of the carbonaceous variables are derived from the thermodynamical relations. The limited number of observations in the Indian Ocean primarily determines the uncertainty of observations-based reconstructed data products such as OceanSODA.

DIC from the models are compared with OceanSODA in the last row of Figure 4. The OTTM shows a low correlation (Figure 4n) throughout the BoB region, but this low correlation is restricted only to the head-bay region in ROMS (Figure 4m). The measurements of DIC fluxes entering to the BoB from rivers are not available, hence, we provide a climatological DIC value corresponding to the nearest grid point from the river mouth. This could result in a low correlation in the BoB head-bay region. High RMSE in the northern BoB and AS is shown by ROMS (Figure 4o), but the rest of the domain has low RMSE.
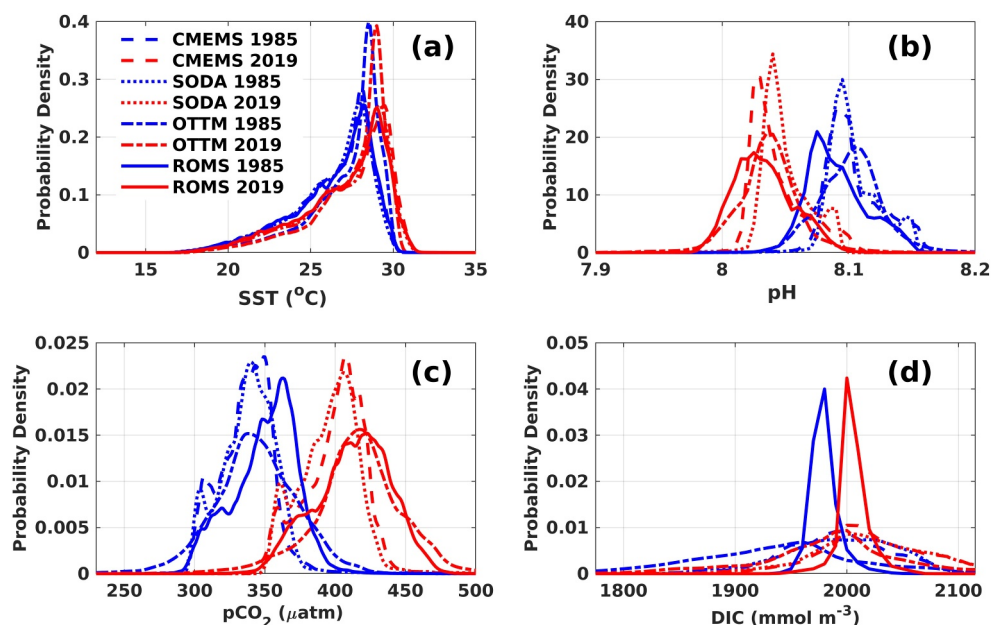
Figure 6. The probability density function of model (ROMS and OTTM) simulated (a) SST, (b) pH, (c) pCO$_2$, and (d) DIC compared to the observations-based products (OceanSODA and CMEMS-LSCE-FFNN).

3.1.4. Consistency With CMEMS-LSCE-FFNN Data

The spatial correlation and RMSE between ROMS (OTTM) and CMEMS-LSCE-FFNN in Figure 5 are similar to that of ROMS (OTTM) and OceanSODA. We observe, from Figures 4a and 5a, that model-simulated SST (ROMS and OTTM (Figures 4b and 5b)) agrees better with CMEMS-LSCE-FFNN SST than OceanSODA SST. However, it is to be noted that both reconstructed data products used SST as a predictor. The low correlation in the central-eastern zone compared with OceanSODA is reduced compared to CMEMS-LSCE-FFNN (Figures 4a and 5a). The comparison of modeled DIC, pCO$_2$, and pH with CMEMS-LSCE-FFNN data indicates similar results as in OceanSODA.

3.2. Comparison of SST and Carbonate System Variables Between 1985 and 2019

The increasing uptake of anthropogenic carbon by the oceans in the changing environment reduces ocean pH. In addition, the increase in Global temperature causes enhanced vertical stratification, resulting in less CO$_2$ out-gassing (reduced upwelling) and reduced transport of excess carbon to the deep ocean. Further, oceanic heat waves cause noteworthy changes in the oceans' biological production and affect the air-sea exchange of gases in a changing environment. Further, ocean warming has a severe impact on the speciation of carbonate chemistry species, which in turn affects pH. These climatic changes are directly related to the changes in ocean pH. This section explores the changes in surface pH, pCO$_2$, DIC, and SST simulated by ROMS (OTTM). We also compare the changes (difference between 2019 and 1985) in pH, SST, DIC, and pCO$_2$ between observations-based reconstructed data products (CMEMS-LSCE-FFNN and OceanSODA) and ROMS (OTTM).

The statistical distributions of SST (for 1985 and 2019) in the IO region, from models (ROMS and OTTM) and SST reanalysis products underlying observations-based pCO$_2$ reconstructions (CMEMS-LSCE-FFNN and OceanSODA), are depicted in Figure 6a. A right shift in the peak of SST in 2019 from 1985 is seen in both ROMS and OTTM as well as in CMEMS-LSCE-FFNN and OceanSODA data products (Figure 6a). This clearly shows that there has been a rise in SST in the IO in the past 34 years (owing to the global warming). The changes in mean SST values between 2019 and 1985 are 0.9°C for SST used as predictor in OceanSODA, 0.93°C for SST used as predictor in CMEMS-LSCE-FFNN, and 0.7°C for ROMS (0.3°C for OTTM) (Table S1 in Supporting Information S1).

The left shift in the peak of pH in 2019 compared to 1985 indicates acidification caused by the global warming and anthropogenic activities in the IO region (Figure 6b). Figure 6b represents the pH distribution from

OceanSODA, CMEMS-LSCE-FFNN, and ROMS (OTTM). Both CMEMS-LSCE-FFNN and ROMS suggest a drop in mean sea-surface pH value between 1985 and 2019 by 0.06 and 0.058 respectively, whereas a drop by 0.054 (0.065) is seen from OceanSODA (OTTM) (Table S1 in Supporting Information S1). Figure 6c shows a right shift in peak, indicating an increase in the sea-surface $p\mathrm{CO_2}$. The change in mean values between 1985 and 2019 is 62.30 (73.2) μatm for ROMS (OTTM), whereas it is 57.20 and 62.40 μatm for OceanSODA and CMEMS-LSCE-FFNN, respectively. Interestingly, the rise in sea-surface $p\mathrm{CO_2}$ seen from ROMS, OceanSODA, and CMEMS-LSCE-FFNN is almost equal to the atmospheric $\mathrm{CO_2}$ rise (as seen from Mauna Loa station) in the same period ($\approx$64 ppm). A similar increment in sea-surface DIC (Figure 6d) is observed from ROMS and the observations-based reconstructed data products of the order of 25–30 mmol m^{-3} (50 mmol m^{-3} for OTTM).

Table S1 in Supporting Information S1 shows a detailed statistical description of the spread of pH, DIC, SST, and $p\mathrm{CO_2}$ in 1985 and 2019. Figure 6 indicates that the distribution of pH, DIC, SST, and $p\mathrm{CO_2}$ for the years 1985 and 2019 derived from model outputs and observations-based data products are low leptokurtic, except for ROMS simulated DIC. DIC (Figure 6d) distribution from ROMS indicates the distribution to be highly leptokurtic (in both 2019 and 1985). The spatial variability of DIC simulated by ROMS is essentially less compared to other reconstructed data products and model outputs used in the analysis. It may be caused due to several factors. We have used the KPP mixing scheme in the present model configuration. This scheme seems to respond differently throughout the regional Indian Ocean to the biogeochemical fluxes. The diffusive thermocline (when compared with in-situ observations) confirms the same (Chakraborty et al., 2019). As a result, bias in the model-simulated physical state of ocean subsequently propagates to model simulated biogeochemical state through the prescribed coupled dynamics. Further, ROMS was initialized using GLODAP data, which itself has a very low spatial variability of DIC since the number of observations available in the Indian Ocean is very limited. On top of that GLODAP is an annual mean climatology, which may not be an ideal initial condition. The river distribution, its discharge, and the amount of nutrients available from rivers are provided climatologically, which is also not ideal. Moreover, the nutrients and carbonate variables (DIC and ALK) from the rivers are estimated from the nearest grid value available from the WOA or GLODAP, hence until a more realistic representation of rivers is not available, the variability of DIC is expected to be less, especially in the BoB region.

In contrast, the observations-based products and OTTM model show the DIC distribution for both years to be low leptokurtic. The mean DIC differs between ROMS and observations-based products by almost 20 mmol m^{-3} for both years (2019 and 1985). This difference in DIC should not affect the driver analysis as this magnitudinal difference seems to be consistent and should have no effect on the trends.

Figures 7a–7d show the difference (between 2019 and 1985) in annual mean SST from ROMS, OTTM along with the predictor SST used in OceanSODA and CMEMS-LSCE-FFNN. The spatial pattern of these differences is similar for both the models (ROMS and OTTM) and the observations-based reconstructed data products (SODA and CMEMS-LSCE-FFNN), but the difference is much lower in the OTTM model. The increase in SST is seen to be relatively lower in ROMS than in observations-based products. The southeastern region is observed to have a decrease in SST in 2019 compared to 1985 (shown by models and observations-based products). We observe the regional spread of low SST values in 2019 concerning 1985 to be higher in the models (ROMS and OTTM) than in OceanSODA and CMEMS-LSCE-FFNN. The northern BoB has lower warming in the ROMS and OTTM, unlike in CMEMS-LSCE-FFNN and OceanSODA.

Figures 7e–7h show a decrease in pH in 2019 compared to 1985 in all four products. The coastal regions of northern AS are observed to have a lower decrease in pH than other regions. The eastern IO region has the lowest change in oceanic pH in ROMS, but the OTTM model shows the reverse. ROMS and observations-based products show that pH reduces less rapidly in the eastern IO region. Similarly, Figures 7i–7k show a high rise in sea-surface $p\mathrm{CO_2}$ in the western region. The OTTM model shows the highest rise of sea-surface $p\mathrm{CO_2}$ in eastern IO. The positive $p\mathrm{CO_2}$ change and large negative values in pH change are due to the DIC increase in OTTM. The increase in $p\mathrm{CO_2}$ shown by ROMS is higher than that of the estimated increase seen in OceanSODA and CMEMS-LSCE-FFNN.

The spatial pattern of the difference in DIC between 2019 and 1985 is relatively similar for ROMS and observations-based products (Figures 7m–7o), while OTTM shows a much higher increase in DIC in the eastern region (Figure 7p). The change in DIC from SODA is slightly higher than in ROMS and CMEMS in the southeastern part of the IO and lower in the Western Equatorial region (Figure 7n). The overall discrepancies in the models and the observations-based products may be attributed to the paucity of required observation of the
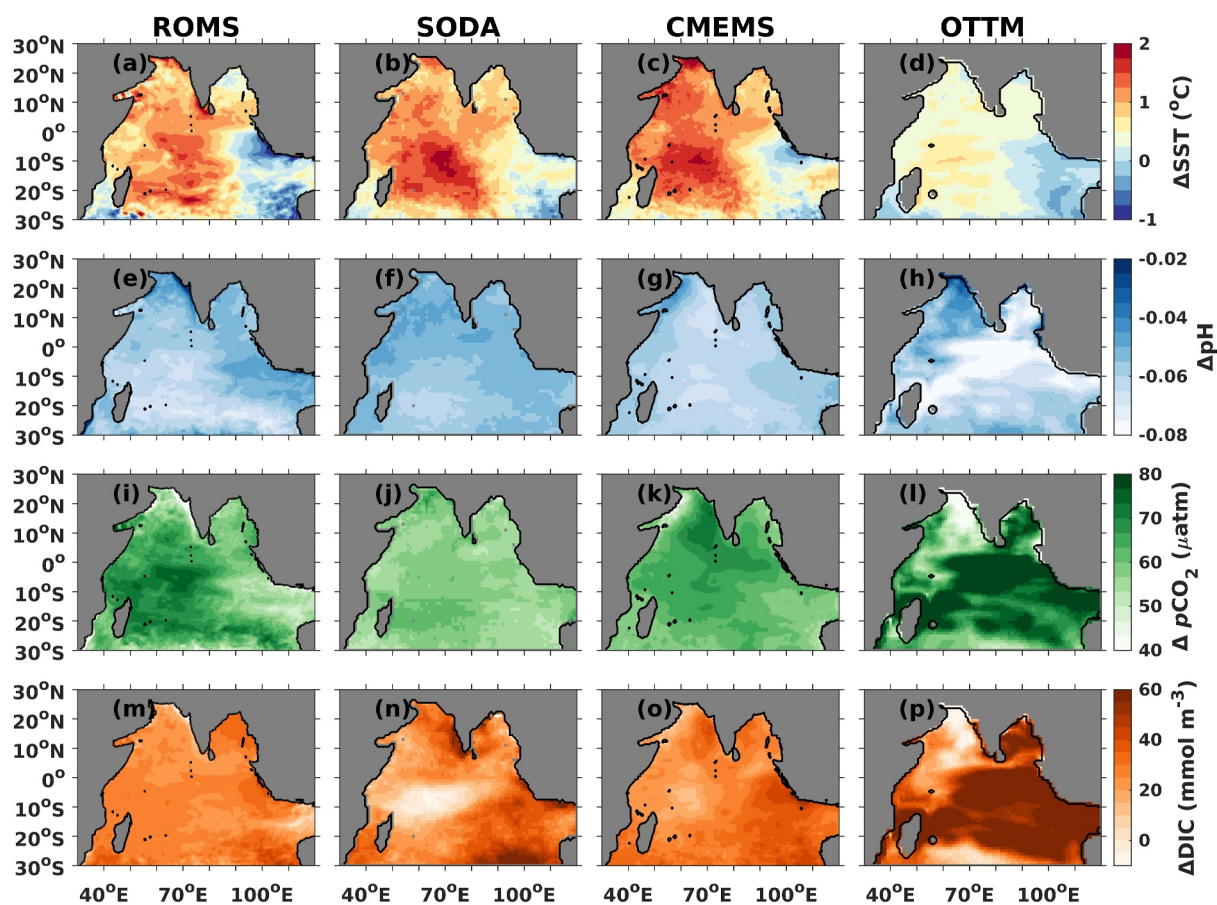
Figure 7. Spatial annual mean difference (between 2019 and 1985) in SST (°C, figures a–d), pH (figures e–h), $p\mathrm{CO}_2$ (μatm, figures i–l), and DIC (mmol m^{-3}, figures m–p) from ROMS (first column), OceanSODA (second column), CMEMS-LSCE-FFNN (third column), and OTTM (fourth column).

carbonate variables in the IO region, along with model biases (e.g., imperfect representation of biology and biogeochemistry interacting with the ocean carbon cycle, model resolution, etc.).

3.3. Interannual Variability

To compare the interannual variability of pH ($p\mathrm{CO}_2$) from ROMS and OTTM with the observations-based products CMEMS-LSCE-FFNN and OceanSODA, we first deseasonalize and detrend the pH ($p\mathrm{CO}_2$) for the IO and its sub-domains (AS, BoB and Equatorial Indian Ocean (EIO)). In Figure 8 (Figure S7 in Supporting Information S1), the deseasonalized and detrended region averaged time-series of pH ($p\mathrm{CO}_2$) is shown for all four products used in this study. The pH ($p\mathrm{CO}_2$) from the OTTM model is observed to have higher values than pH ($p\mathrm{CO}_2$) from other products (Figures 8 and S7 in Supporting Information S1). From Figure 8, we observe that pH from the OceanSODA model has low trough values at certain times, which are absent from pH from other products. Such troughs are also absent for $p\mathrm{CO}_2$ from OceanSODA (Figure S7 in Supporting Information S1).

Table 2 (Table S4 in Supporting Information S1) shows a statistical comparison of model-simulated (ROMS and OTTM) pH ($p\mathrm{CO}_2$) with the observations-based products (CMEMS-LSCE-FFNN and OceanSODA). The interannual variability of pH ($p\mathrm{CO}_2$) simulated by ROMS shows better agreement with the interannual variability of pH ($p\mathrm{CO}_2$) from CMEMS-LSCE-FFNN and Ocean SODA than OTTM-based pH ($p\mathrm{CO}_2$). The correlation with observations-based fields and corresponding RMSE for ROMS-generated pH ($p\mathrm{CO}_2$) are consistently better than the OTTM model throughout the IO and its subdomains. This result highlights that a high-resolution regional model is capable of capturing the key processes controlling the interannual variability of pH better than a coarse resolution global model on a regional scale. Based on the synthesis of 12 global and two regional model simulated outputs, Sarma et al. (2023) showed that the high-resolution regional models perform relatively better than the
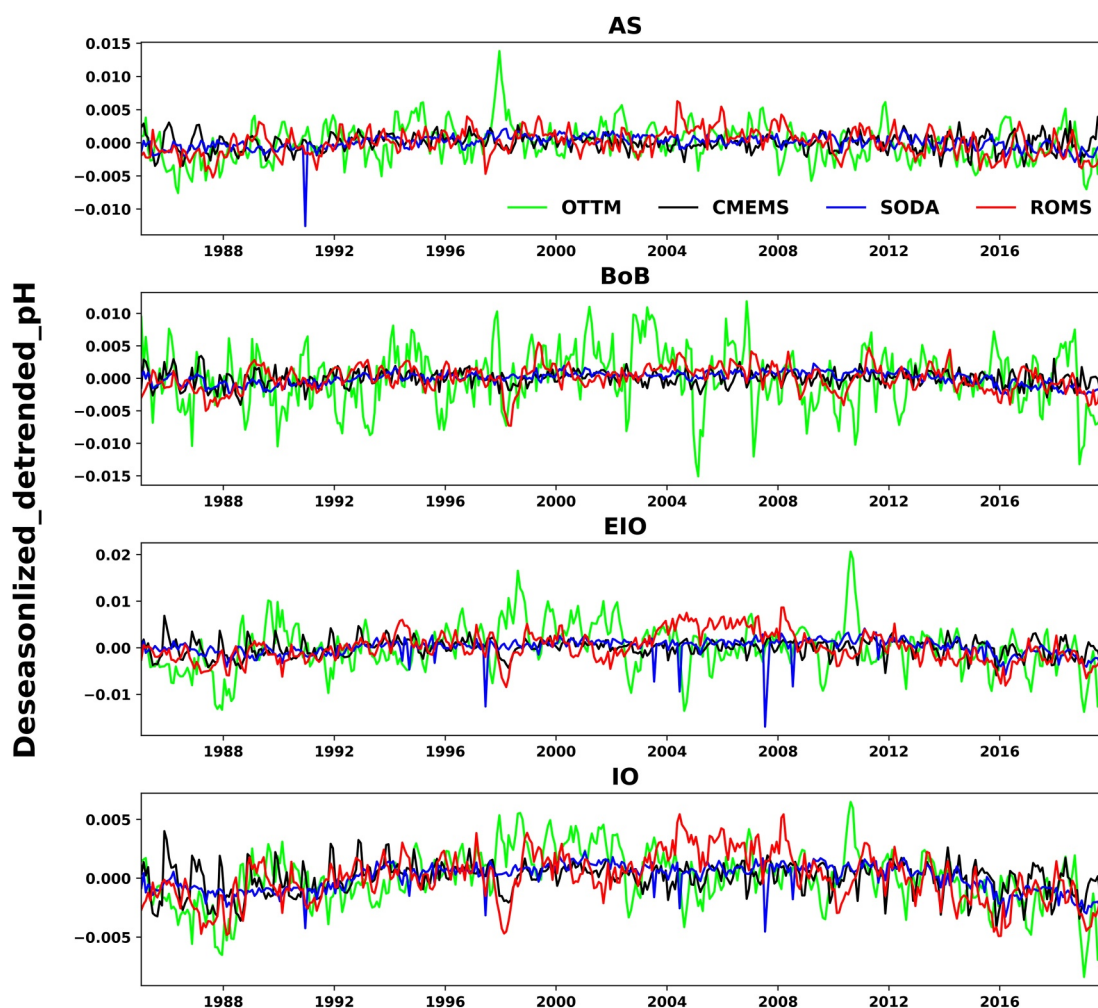
Figure 8. Comparison of interannual variability of pH in the IO region and its subdomains (AS, BoB, and EIO) between observations-based products (SODA and CMEMS-LSCE-FFNN) and models (ROMS and OTTM).

coarse resolution global models in the Indian Ocean due to an improved representation of key processes controlling the air-sea CO_2 flux variability in the regional models. It is evident that a high horizontal resolution regional model can capture the mesoscale processes better than a coarse resolution global model. Hence, high-resolution regional models like ROMS used in this study are required to understand the interannual spatial and temporal variabilities on a regional scale.

3.4. Long-Term Trend Analysis in Different Regions of IO

In this section, we report the trends in pH (pCO_2) and DIC for the IO and also separately for AS, BoB, and EIO. Table 3 shows ROMS-simulated trends (having 95% significance) of DIC, pH, and pCO_2 for each decade over the period 1980 to 2019. The trend is calculated at all the spatial grid points. Then, the grids are identified as having at least 95% significance in the trend. Finally, the trend in each of these grid points is averaged to represent the mean trend of the region under consideration and the uncertainty bars represent the spatial STD in the trends.

Further, we compare model-simulated (ROMS and OTTM) trends with trends estimated from OceanSODA and CMEMS-LSCE-FFNN data products (the grids having trends above 95% significance are selected while calculating the trend for a region). We select the common data-availability period between ROMS (OTTM), OceanSODA, and CMEMS-LSCE-FFNN, that is, 1990–2019, and compare the pH trends for the three decades of this period (Figure 9). We observe that the estimates of pH trend from OceanSODA, CMEMS-LSCE-FFNN, and ROMS match well whereas the estimates of pH trend from OTTM differ (Figure 9). A steeper decrease is

Table 2
Statistical Comparison of the Deseasonalized and Detrended pH Between Models (ROMS and OTTM) and Observations-Based Products (CMEMS-LSCE-FFNN and OTTM)

	Correlation	RMSE
Arabian Sea		
ROMS versus OceanSODA	0.18	0.002
OTTM versus OceanSODA	0.12	0.003
ROMS versus CMEMS-LSCE-FFNN	0.11	0.002
OTTM versus CMEMS-LSCE-FFNN	0.01	0.003
Bay of Bengal		
ROMS versus OceanSODA	0.35	0.001
OTTM versus OceanSODA	0.14	0.004
ROMS versus CMEMS-LSCE-FFNN	0.23	0.001
OTTM versus CMEMS-LSCE-FFNN	0.04	0.004
Equatorial Indian Ocean		
ROMS versus OceanSODA	0.31	0.003
OTTM versus OceanSODA	0.21	0.005
ROMS versus CMEMS-LSCE-FFNN	0.34	0.003
OTTM versus CMEMS-LSCE-FFNN	0.01	0.005
Indian Ocean		
ROMS versus OceanSODA	0.55	0.001
OTTM versus OceanSODA	0.46	0.002
ROMS versus CMEMS-LSCE-FFNN	0.44	0.001
OTTM versus CMEMS-LSCE-FFNN	0.19	0.002

observed in AS in ROMS and OceanSODA than in CMEMS-LSCE-FFNN and OTTM. During 1990–1999 in AS, the pH trend from the ROMS and OceanSODA (Table S6 in Supporting Information S1) are -0.012 ± 0.0027 dec^{-1} and -0.012 ± 0.002 dec^{-1}, which are lower than the pH trend shown in CMEMS-LSCE-FFNN (-0.016 ± 0.001 dec^{-1}) and OTTM (-0.015 ± 0.004 dec^{-1}). In the subsequent decade in AS, 2000–2009, the rate of decrease is seen to be lowest in ROMS (-0.014 ± 0.002 dec^{-1}) and highest in CMEMS-LSCE-FFNN (-0.019 ± 0.002 dec^{-1}) and OTTM (-0.019 ± 0.006 dec^{-1}). In the recent decade (2010–2019), the rate of pH decrease simulated by ROMS is highest (-0.021 ± 0.002 dec^{-1}), and the rates of OceanSODA and CMEMS-LSCE-FFNN are almost the same in AS.

In the BoB, the decreasing trend of pH simulated by ROMS (-0.015 ± 0.003 dec^{-1} during 1990–1999, and -0.015 ± 0.002 dec^{-1} during 2000–2009) is higher than OceanSODA and lower than CMEMS-LSCE-FFNN for the first two decades. The OTTM pH trends (-0.027 ± 0.011 dec^{-1}) considerably diverge from the rates shown by ROMS, OceanSODA, and CMEMS-LSCE-FFNN for 2000–2009 in the BoB. In EIO, the pH trend simulated by ROMS and estimated from OceanSODA is almost the same during 1990–1999 (-0.012 ± 0.004 dec^{-1}). In the subsequent decade, there is a slight increase in ROMS simulated pH trend (-0.011 ± 0.002 dec^{-1}) but CMEMS-LSCE-FFNN shows a clear decrease in pH trend.

In EIO, during 2010–2019, a high decrease in pH trend is observed for all products. OTTM model shows the highest rate of pH decrease. Interestingly, ROMS and CMEMS-LSCE-FFNN show the same rate of decreasing pH trend in the recent decade. For the complete IO region, the pH trends in OceanSODA and ROMS are almost the same (Figure 9). Although CMEMS-LSCE-FFNN shows a similar decreasing pattern, the magnitude of change in trends is slightly different. An acceleration of pH trend in the last decade is common in all models and observations-based products. Lo Monaco et al. (2021) show

Table 3
Slope (Rate of Change) for Decadal Intervals (10 Years) of ROMS, Averaged Over AS, BOB, EIO, and IO Regions

Regions	Decades	pH(units dec^{-1})	pCO_2(μatm dec^{-1})	DIC(mmol m^{-3} dec^{-1})
AS	1980–1989	-0.01 ± 0.007	10.48 ± 8.65	5.68 ± 7.39
	1990–1999	-0.012 ± 0.003	13.31 ± 2.84	7.97 ± 1.39
	2000–2009	-0.014 ± 0.002	15.88 ± 2.13	9.57 ± 2.20
	2010–2019	-0.021 ± 0.002	23.84 ± 2.42	7.24 ± 1.74
BoB	1980–1989	-0.009 ± 0.002	9.60 ± 1.32	6.95 ± 1.51
	1990–1999	-0.015 ± 0.003	15.72 ± 2.79	10.26 ± 1.47
	2000–2009	-0.016 ± 0.002	17.17 ± 2.11	11.46 ± 1.25
	2010–2019	-0.018 ± 0.003	20.94 ± 2.76	6.73 ± 1.54
EIO	1980–1989	-0.011 ± 0.002	11.81 ± 1.89	11.10 ± 2.11
	1990–1999	-0.012 ± 0.004	12.95 ± 4.02	10.15 ± 2.32
	2000–2009	-0.011 ± 0.002	12.86 ± 2.85	4.22 ± 6.67
	2010–2019	-0.018 ± 0.004	21.82 ± 4.19	12.21 ± 6.39
IO	1980–1989	-0.011 ± 0.00	11.56 ± 4.18	10.81 ± 4.55
	1990–1999	-0.013 ± 0.004	14.07 ± 3.87	10.04 ± 2.54
	2000–2009	-0.014 ± 0.004	15.58 ± 3.48	6.69 ± 7.19
	2010–2019	-0.019 ± 0.004	22.67 ± 4.19	13.29 ± 7.69
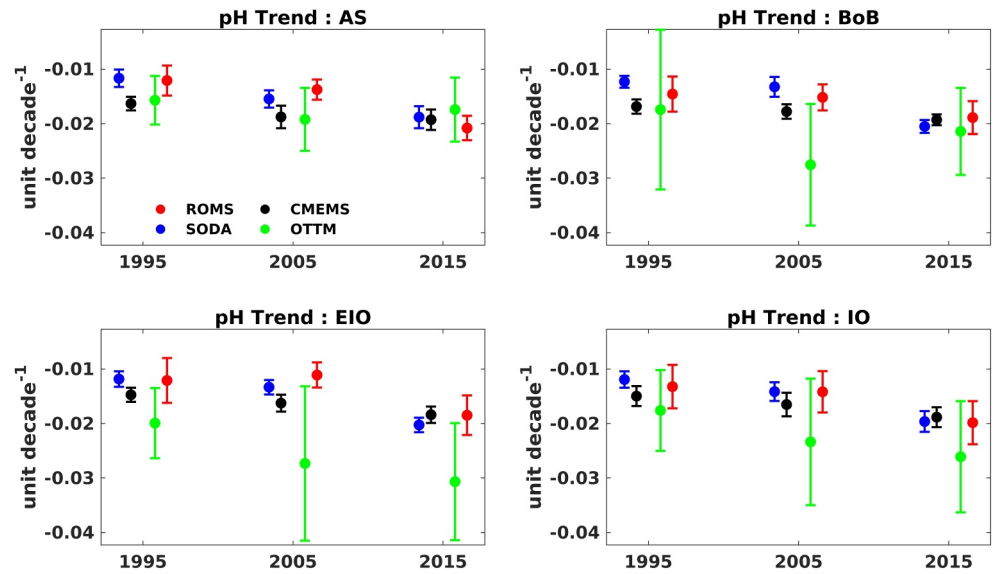
Figure 9. Decadal trend of pH in AS, BoB, EIO, and IO regions. The years 1995, 2005, and 2015 denote the center of 1990–1999, 2000–2009, and 2010–2019. The uncertainty bars represent the standard deviation of region averaged trend values with 95% significance.

a similar acceleration of pH trend (-0.0243 dec^{-1}) in the Mozambique channel for the period 2004–2019. Interestingly, the ROMS result shows a similar magnitudinal increase in the decreasing pH trend (≈ -0.02 dec^{-1}) for all the regions (Table 3) in the last decade. Similarly, the pCO$_2$ trends for each region are shown in supplementary, which reveals that pCO$_2$ increasing trends simulated by ROMS and estimated from OceanSODA are close to each other (Figure S3 in Supporting Information S1).

The DIC in the ocean is steadily increasing by the continuous uptake of anthropogenic CO$_2$ emitted to the atmosphere. The Indian Ocean region is second to the South Pacific in terms of increase in anthropogenic carbon storage (Müller et al., 2023). The anthropogenic carbon storage is reported to increase at 7.2 ± 0.9 from 1994 to 2004 and 5.7 ± 0.6 Pg C dec^{-1} from 2004 to 2014 (Müller et al., 2023). As DIC is the primary driver controlling
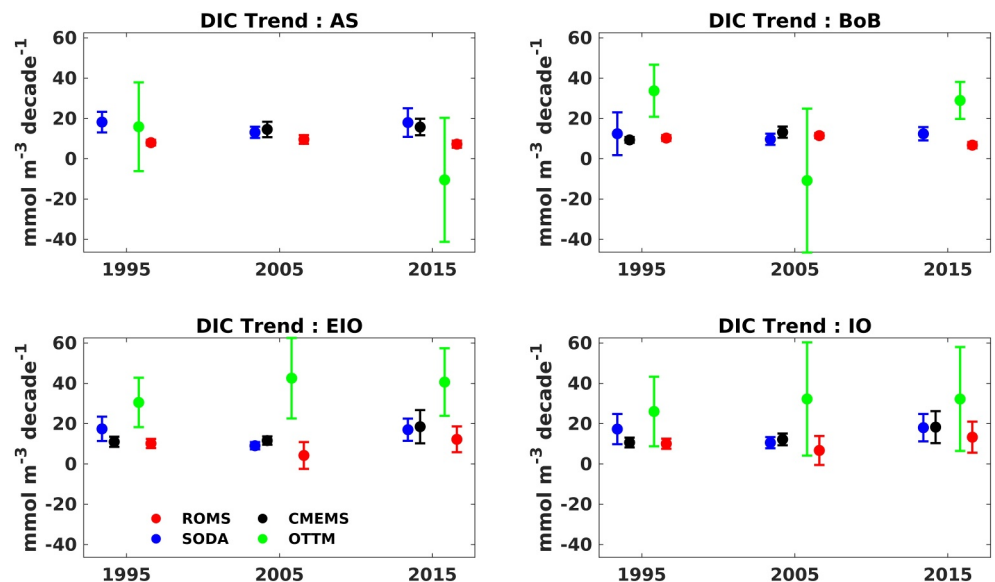
Figure 10. Decadal trend of DIC in AS, BoB, EIO, and IO regions. The years 1995, 2005, and 2015 denote the center of 1990–1999, 2000–2009, and 2010–2019.

trends of pH and $p\mathrm{CO_2}$, we look at the decadal trends of DIC in AS, BoB, EIO, and IO regions from all the products (Figure 10).

Interestingly, the variation of DIC trends in AS and BoB from OceanSODA and the ROMS are opposite. The ROMS shows that the DIC trend increased in the northern Indian ocean during 2000–2009 period (9.57 ± 2.18 mmol m^{-3} dec^{-1} in AS and 11.46 ± 1.25 mmol m^{-3} dec^{-1} in BoB) than 1990–1999 (7.97 ± 1.39 mmol m^{-3} dec^{-1} in AS and 10.26 ± 1.47 mmol m^{-3} dec^{-1} in BoB). The trend in DIC again decreases in the third decade (7.24 ± 1.74 mmol m^{-3} dec^{-1} in AS and 6.73 ± 1.54 mmol m^{-3} dec^{-1} in BoB).

The CMEMS-LSCE-FFNN had no significant trend during 1990–1999 in the AS and 2010–2019 in BoB (Figure 10). Similarly, no significant trend in AS is found between 2000 and 2009 for the OTTM model (Figure 10). The DIC trends in the EIO region by Ocean-SODA and the ROMS are synchronous, that is, high in 1990–1999 and 2010–2019, while low in 2000–2009, whereas OTTM showed a much higher DIC trend in 2000–2009. The lower DIC trend in the EIO region during 2000–2009 is also reflected in the $p\mathrm{CO_2}$ trends (Figure S4 in Supporting Information S1). Results from Ocean-SODA, CMEMS, and ROMS indicate that the $p\mathrm{CO_2}$ trends appeared stable over 1990–2009 (i.e., not tracking the rising of atmospheric $\mathrm{CO_2}$), and accelerated in 2010–2019 ($p\mathrm{CO_2}$ trend > +2 μatm yr^{-1} for all models, Figure S4 in Supporting Information S1). The low DIC trend 2000–2009 from ROMS ($+0.4 \pm 0.08$ μmol kg^{-1} yr^{-1}) is about half the expected $\mathrm{C_{ant}}$ trend (+1 μmol kg^{-1} yr^{-1}). In the southwestern IO, Metzl et al. (2022) evaluated a trend of $+1.05 \pm 0.08$ μmol kg^{-1} yr^{-1} in the subsurface. A calculation of $\mathrm{C_{ant}}$ concentrations based on the TrCOCA method (Touratier et al., 2007) using the GLODAP data available in the EIO region over 1978–2020 leads to a $\mathrm{C_{ant}}$ trend of $+0.86 \pm 0.10$ μmol kg^{-1} yr^{-1} in the subsurface (Figure S9 in Supporting Information S1). The low DIC trend in the EIO region during 2000–2009 represents an anomaly that could be explained by natural processes that would counteract the DIC increase due to the progressive $\mathrm{C_{ant}}$ accumulation. After 2010, the system is back to a high DIC trend in the EIO and the pH trends are the same for ROMS, SODA, and CMEMS (average of −0.019 per decade). Hence, there is a corresponding rise in the pH trend in the IO region from 2000 to 2009 (Figure 9). However, the link between the storage of anthropogenic carbon and surface DIC needs further investigation. The link between surface changes to the inventories is related to the exchange of properties between mixed layer to thermocline and deeper ocean with expected inventory changes due to biological export and redistribution pathways of the tracers in the deep. It is also observed that although the decadal trends in pH and $p\mathrm{CO_2}$ in the ROMS and OceanSODA were reasonably close, the DIC trend does have differences in magnitude.

3.5. Effect of ENSO and IOD on the Indian Ocean Acidification

In this section, we perform the EOF analysis as described in Section 2.3.3 to understand the effect of ENSO and IOD on the interannual variability of ocean acidification in the IO region. Figure 11a shows a negative spatial pattern of pH (positive spatial pattern for $p\mathrm{CO_2}$ in Figure S6a in Supporting Information S1) anomalies. The corresponding PC-1 shows a negative correlation (−0.52 with 99% significance) between the pH anomalies and the Nino3.4 index, and a positive correlation between the $p\mathrm{CO_2}$ anomalies and the Nino3.4 index. Further, PC-1 of pH anomalies and DMI index shows a moderate negative correlation (−0.37 with 99% significance) whereas $p\mathrm{CO_2}$ anomalies and DMI index has a moderate positive correlation. The first mode is found to explain 18.44% of the variance. Therefore, it is evident from EOF-1 mode and associated PC-1 that ENSO dominantly influences the IO pH variability ($p\mathrm{CO_2}$ variability as well). The basin-wide warming during the El Niño increases the free H$^+$ ions and $p\mathrm{CO_2}$, shifting toward lower pH values. However, the moderate correlation of PC-1 with DMI indicates the combined influence of ENSO and IOD on ocean acidification.

Figure 11b shows a negative spatial pattern of pH (positive spatial pattern of $p\mathrm{CO_2}$ anomalies as shown in Figure S6b in Supporting Information S1) anomalies in the east and a positive in the west. The corresponding PC-2 shows a moderate negative (positive for $p\mathrm{CO_2}$ anomalies as shown in Figure S6d in Supporting Information S1) correlation (−0.30 with 99% significance) with the DMI index, indicating the influence of IOD (Figure 11d). PC-2 correlates poorly (for both pH and $p\mathrm{CO_2}$ anomalies) with Nino3.4, indicating no influence of ENSO on the second mode. The second mode explains 8.56% of the total variance. Hence, although from EOF-1 mode the impact of ENSO dominance on the IO pH variability is evident, the influence of IOD is spread across EOF-1&2 modes. The positive IOD often enhances upwelling in the eastern coastal region, which brings the low pH (high $p\mathrm{CO_2}$) sub-surface waters to the surface. Thus, the strength of El Niño could affect the ocean
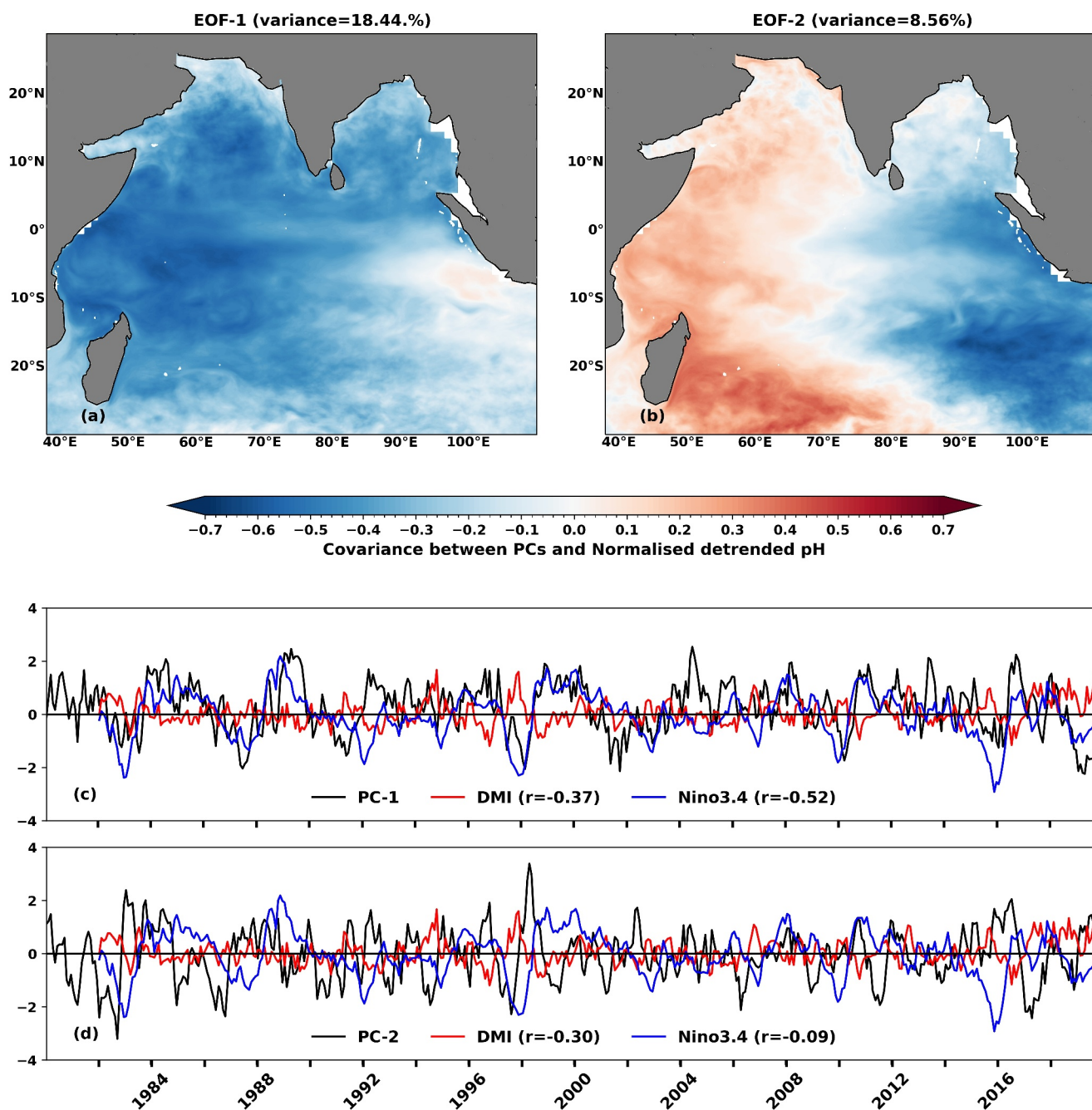
Figure 11. The figures (a, b) show EOF-1 and EOF-2 of pH in terms of covariance (from ROMS). Figures (c, d) show the statistical comparison of the first two principal components (PC-1 and PC-2) with Nino3.4 and DMI indices.

acidification of the IO region. As the strength increases, the basin-wide warming could increase, resulting in more acidified IO in the future.

3.6. Effect of Each Driver on pH and pCO$_2$ Trends in Different Regions of the Indian Ocean

In this section, we analyze the effect of the trends of each driver (DIC, SST, SSS, and ALK) on the trend of pH and pCO$_2$ individually for the past four decades followed by the entire 40 years (1980–2019) separately for the AS, BoB, and EIO regions and the IO basin using ROMS simulated outputs. Figure 12 represents the percentage contribution of each driver on the pH trends (similar contributions on pCO$_2$ trends can be seen in Figure S8 in
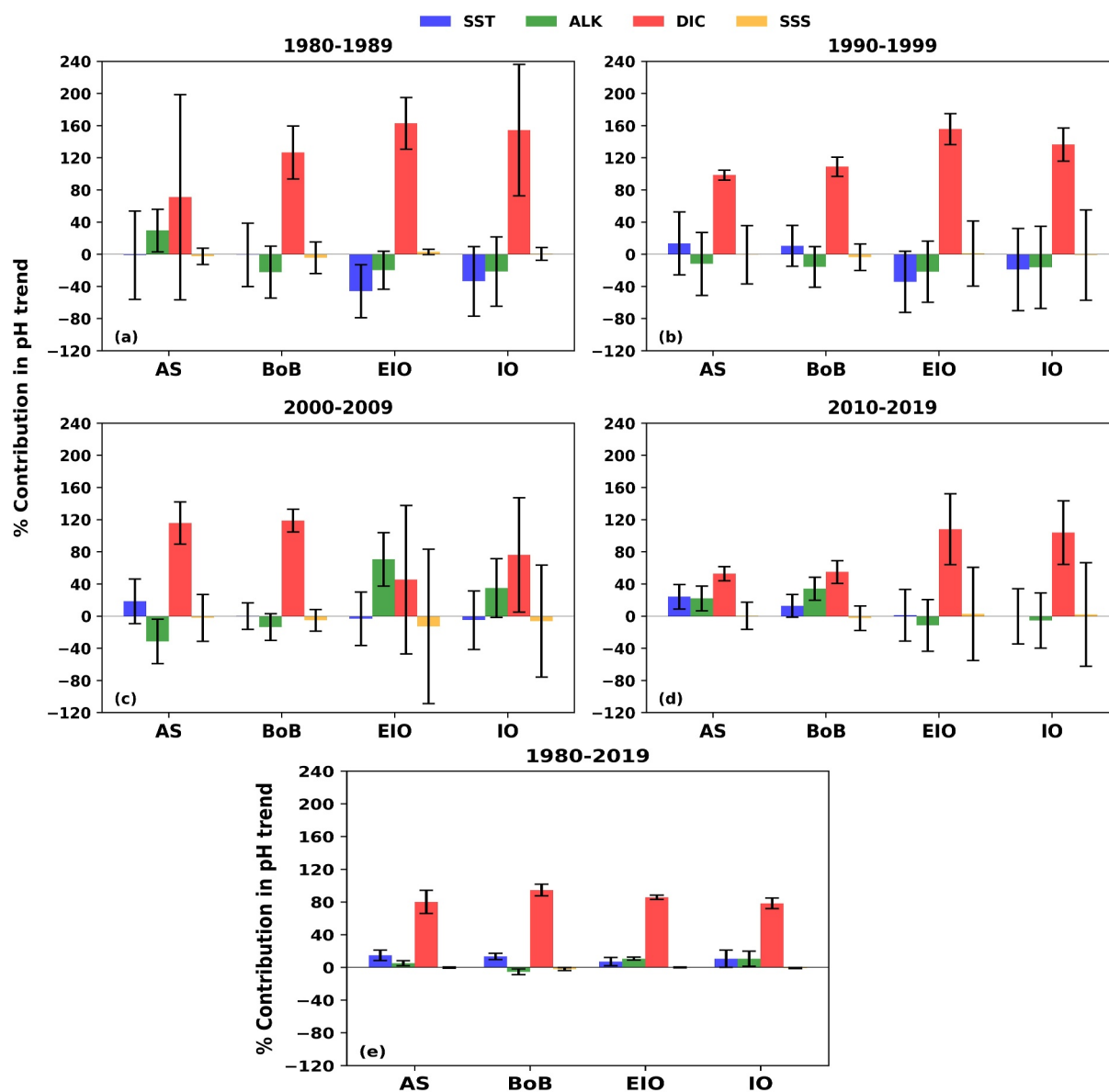
Figure 12. Percentage contribution of each driver (with standard deviation shown by error bars) on the trend of pH individually for the four decades (a–d), and for the entire 40 years period (1980–2019) (e).

Supporting Information S1). The method to quantify the effect of each driver on pH (pCO_2) trends is described in Section 2.3.2.

Figure 12 shows that in the AS, DIC trends primarily control ocean acidification (OA) trends during each of the past four decades (71.1%, 98.5%, 115.9%, and 52.9% (Figures 12a–12d)) and also the net 40 years trend (Figure 12e). The ALK trends contribute to enhancing OA during 1980–89 (Figure 12a) and 2010–19 (Figure 12d). While it acts as a buffer to the relative enhancement of OA rates during 1990–99 (Figure 12b) and 2000–09 (Figure 12c). Further, the buffering effect caused by the contribution of ALK is more crucial during 2000–09 (Figure 12c).

The SST rise due to global warming consistently affects the OA trends in the AS (Figure 12). During 1980–89, the SST played almost no role in moderating the OA trends (−1.1%), but from 1990 to 99, the SST contributed to the increasing OA trend (13.6%). The contribution of SST trends toward decreasing pH trends has consistently increased till the recent decade (2010–19) (Figures 12a–12d). In the recent decade, the three major drivers (SST,

DIC, and ALK) have been found to collectively increase the OA in the AS (SSS has negligible effect (0.5%)). This indicates that the global warming and anthropogenic carbon storage increase in the future will lead to an increase in acidity (a measure of H$^+$) of the surface waters of AS. We also observe that the AS acidifies much faster in the recent decade than in the past three decades (Table.3). Sreeush et al. (2019) reported an exacerbation of acidification by 16% in the AS due to the SST warming alone, which is found to be consistent with the contribution of SST derived from ROMS outputs (Figure 12e).

Although the decadal rates of OA for AS and BoB are similar, the drivers controlling the acidification rates are different. During 1980–89, DIC was the only driver increasing the rate of OA in the BoB (126.7%). The ALK was found to be the second important driver, which buffers the OA rates (−22%), reducing the magnitude of the negative slope. SSS (though very low compared to DIC and ALK, −4.2%) also acts as a buffer to the OA. During 1990–99, ALK again buffers OA (−15.6%) in the BOB, but DIC and SST both positively contribute to the rate of pH decrease (108.9% and 10.6%). The influence of SST is almost completely neutralized by ALK, leaving DIC as a major contributor to the rising OA rates during 1990–99.

For the BoB, the role of drivers controlling the OA rates in the first (1980–89) and third (2000–09) decades are almost similar, that is, DIC is the major contributor to the rise in OA, and ALK buffers these increasing rates. ALK has acted differently in the recent decade (2010–19) compared to the past three decades. In this decade, ALK enhances the rates of OA (34.1%) in BoB along with DIC (54.9%) and SST (12.9%). In BoB, the buffering of OA rates has consistently decreased from the first (1980–89) to the last decade (2010–19). This could be due to the variation in the stratification strength (which influences productivity in surface and near-surface waters) of the BoB from 1980 to 2019 (Joshi et al., 2021; Takahashi et al., 2014). The influence of drivers on pH trends over the 40 years shows that SST is the second most crucial driver controlling pH trends after DIC in the AS and BoB (14.8% and 13.4%; Figure 12e). The ALK is seen to have a buffering effect on pH decrease in the BoB (−5.4%), whereas it positively contributes to pH decrease in AS (5%).

During 1980–89, the contribution of SST in controlling OA trends, both in the AS and BoB, was insignificant, whereas, in the EIO, SST was found to decelerate the negative slope of pH (−45.8%). Further, in the EIO, the contribution of SST in balancing the pH trends was found to be more compared to the contribution of ALK (−19.7%) during 1980–89 (Figure 12a). DIC (162.9%) remained the primary contributor to the increasing OA rates in EIO.

In the EIO, the effect of all drivers remained the same during 1990–99 as it was in 1980–89, but ALK (70.7%) became the primary driver of the pH trend during 2000–09 (Figure 12c). ALK was found to have a negative slope in the EIO during 2000–09. As a result of which, instead of buffering, it primarily enhanced the OA rates. DIC (45.4%) acts as a secondary driver, enhancing the OA rates during 2000–09. Further, in the EIO, SST's buffering effect or deceleration of negative pH slope from 1980 to 1999 (−45.8% and −34.2% during 1980–89 and 1990–99, respectively) became almost negligible during 2000–09 (−3.1%). SSS played a major buffering role in 2000–09 (−12.7%), which is the greatest contribution of SSS on the OA trends in the IO throughout 1980–2019. The decrease in SSS and thus ALK in the EIO is attributed to the combined effect of variations in local precipitation and freshwater transport through ITF during 2000–2009 (Li et al., 2023). Based on a series of numerical experiments (interestingly using a high-resolution ROMS), Li et al. (2023) showed that the primary driver controlling SSS variability in the EIO during 2000–2010, is local precipitation, whereas the contribution of local winds and evaporation is insignificant. Further, they showed that the SSS in the southern EIO increased between 2000 and 2005 but decreased strongly from 2005 to 2011. The increase of local precipitation (resulting in decreasing SSS) during 2005–2011 was attributed to Ningaloo Nino condition.

During the recent decade (2010–2019), the DIC (108.2%) again dominates the increasing OA rates in the EIO. The ALK (−11.4%) is the secondary driver that buffers the OA trend, but the effect is small compared to the DIC. Further, we observe a higher negative pH trend during 2010–2019 due to ALK's weak buffering contribution in the EIO (Table 3). The contrasting change in the contribution of ALK in the recent decades further exacerbates OA rates in the EIO. The contribution of ALK in controlling pH trends in the EIO over the 40 years (1980–2019) indicates that the ALK is positively contributing to enhancing OA rates in the EIO (10.7%). The positive contribution of ALK to OA could be due to the biological influence in EIO (Madkaiker et al., 2023). When a soft tissue pump occurs, in addition to decreasing the concentration of DIC, the formation of organic matter also decreases the concentration of the free protons, [H$^+$], and therefore increases alkalinity (Brewer et al., 1975; Sarmiento & Gruber, 2006). Thus, the contribution of ALK can be positive or negative in the total trends of pH

depending on the strength of biological pumps (Madkaiker et al., 2023). Although ALK dominates OA after DIC in EIO, the role of SST (7%) is also considerable. Therefore, it can be inferred that all three drivers, DIC, ALK, and SST, strongly influence the pH trends in the EIO. Although SSS's influence is negligible, it plays a vital role in modifying surface ALK (Madkaiker et al., 2023).

Table S5 in Supporting Information S1 shows that, from 1980 to 2019, the whole IO region is acidifying at -0.015 ± 0.001 units dec^{-1}. The net trend for pH (1980–2019) in the IO is dominated by DIC (78.3%), followed by SST and ALK (SSS contribution is negligible) (Figure 12e). For the entire IO region, DIC (154.5% (1980–89) and 136.5% (1990–99)) remains the primary driver of the OA trend, followed by SST (-33.5% (1980–89) and -18.8% (1990–99)) during 1980–89 and 1990–99. SST and ALK (-21.4% (1980–89) and -16.2% (1990–99)) both buffer the pH decrease during the first two decades. During 2000–09, the ALK, along with DIC, increases the OA rates, possibly due to the positive contribution from the EIO (Figure 12e) sub-region. The contributions of SST (-0.1%) and SSS (-5.3%) are almost negligible during 2010–19. Thus, DIC (103.9%) is the primary contributor to the increasing OA during the last decade. Hence, this analysis indicates that detailed long-term measurements of ALK and DIC are critical to investigating OA changes throughout the IO region.

4. Summary and Conclusions

This study attempts to model and explore the drivers affecting the long-term variability in sea-surface pH and pCO$_2$ in the IO region. In this study, we divide the IO region into three sub-regions: AS, BoB, and EIO to examine the present status of Indian Ocean acidification more comprehensively. The trends in each sub-region are explored from ROMS (OTTM) and observations-based data products like OceanSODA and CMEMS-LSCE-FFNN.

The comparison between ROMS and OTTM simulated pH and pCO$_2$ with in-situ measurements from BOBOA mooring and SOCAT database indicates that ROMS is more capable of satisfactorily simulating the Indian Ocean carbon dynamics. In addition to in-situ observations, we have compared ROMS and OTTM simulated carbon variables (pH, pCO$_2$, and DIC) with recently developed observations-based reconstructed data products. The results of model validation exercises indicate that the high-resolution ROMS provides a plausible reconstruction of the physics and carbonate chemistry of the IO when forced by reanalysis. Therefore, the high-resolution regional ROMS simulated long-term outputs are subsequently used to understand the spatial and temporal changes of IO pH and to identify the mechanisms and drivers controlling the changes in pH.

Further analysis shows the warming of the sea surface between 1985 and 2019. ROMS shows a shift in the SST mean from 26.27°C in 1985 to 26.97°C in 2019. In the presence of surface warming, we find a change in oceanic pH (8.09 in 1985 to 8.03 in 2019) and associated carbonate variables such as surface pCO$_2$ (350 μatm in 1985 to 412 μatm in 2019) and surface DIC (1979 mmol m^{-3} in 1985–2005 mmol m^{-3} in 2019). The spatial comparison between the annual mean SST, pH, DIC, and pCO$_2$ shows a decrease in surface warming in the southeastern region (extremely influenced by the Indonesian Throughflow dynamics) but a relative increase in ocean acidification. However, the rise in pCO$_2$ and DIC between 1985 and 2019 is almost consistent throughout the IO domain.

The analysis to identify drivers indicates that DIC is the dominant factor controlling the trends of OA in the IO region. However, for the sub-regions (such as AS, BoB, and EIO), DIC and SST are the dominant drivers controlling pH trends in AS and BoB, whereas DIC and ALK are dominating drivers in the EIO. Further, in the EIO region, the effect of SST is prominent in controlling pH trends. An increase in the strength of biological pump is identified as a possible reason for the increased contribution of ALK in the EIO (Madkaiker et al., 2023). The contribution of ALK in controlling pH trends became primary during 2000–09 in the EIO; otherwise, the dominance of DIC in controlling pH trends was evident throughout all decades and in all the sub-regions of IO. These results highlight the need for long-term measurements of DIC and ALK in the IO to better quantify drivers' contribution in controlling OA in the IO region.

The analysis to estimate the changes in pH trends shows a decreasing pH trend throughout the entire IO domain between 1980 and 2019. The pH decreases at a rate of -0.015 ± 0.002 dec^{-1} in AS, $-0.014 \pm 5.74e{-}04$ dec^{-1} in BoB, and -0.015 ± 0.001 dec^{-1} in EIO. The DIC rate is seen to be high during 1990–1999 (10.04 $\pm$ 2.53 mmol m^{-3} dec^{-1}) and 2010–2019 (13.29 $\pm$ 7.69 mmol m^{-3} dec^{-1}), but lower in 2000–2009 (6.69 $\pm$ 7.19 mmol m^{-3} dec^{-1}).

The primary limitation of this study is the lack of a sufficient number of observations in the IO for quantifying the models' errors in spatial and temporal scales. This induces considerable uncertainty in the estimated trends in

ocean acidification. A comparison with OceanSODA and CMEMS-LSCE-FFNN is performed to assess if the spatial variability and trends of ocean acidification simulated by ROMS are similar to those of these recent observations-based reconstructed data products. The contribution of drivers toward pCO_2 trends in different regions shown in this study slightly differs from the results reported in Mohanty et al. (2024) (especially in the EIO and BoB regions). Here it is to be noted that the spatial resolution of CMIP Earth System Models is too coarse to adequately simulate regional ocean dynamics. This is especially true for the regional IO, which experiences a seasonal reversal of winds and associated surface currents, intense upwelling at its western boundary in the AS, extensive riverine runoff in the BoB and freshwater-induced stratification, the IOD, the Indonesian through-flow, etc. that results in a unique physical and biogeochemical dynamics in this region. Further, an improved representation of key ocean processes in the regional models compared to global coarse resolution models resulted in a better simulation of regional ecosystem dynamics and biogeochemical cycles. Sarma et al. (2023) showed that regional high-resolution models better simulate regional ocean dynamics than low-resolution global models. Therefore, identifying drivers and their contributions toward controlling IO acidification reported in this study is more acceptable than the estimates available from coarse-resolution global models. Further, the high-resolution regional models, like ROMS initialized and forced with bias-corrected and downscaled CMIP Earth System Model outputs, are expected to provide a better estimate of the predicted future of regional surface pCO_2 and pH changes than the estimates available from the coarse-resolution global CMIP models. Additionally, studying Aragonite depth and subsurface biogeochemistry with links to the coral growth and species would be the next step in the Indian Ocean analysis.

Conflict of Interest

The authors declare no conflicts of interest relevant to this study.

Data Availability Statement

BOBOA (Sutton et al., 2014, 2019) mooring data is available at https://www.pmel.noaa.gov/co2/story/BOBOA. The SOCAT data (Bakker et al., 2016, 2022) is obtained from https://www.socat.info/index.php/data-access/, and the OceanSODA data (Gregor & Gruber, 2021) can be obtained from https://www.ncei.noaa.gov/data/oceans/ncei/ocads/data/0220059/. CMEMS-LSCE-FFNN data (Chau et al., 2024) is downloaded from https://doi.org/10.14768/a2f0891b-763a-49e9-af1b-78ed78b16982. The high-resolution regional model (ROMS) simulated data (Chakraborty, 2024) used in this study can be downloaded from https://zenodo.org/records/11670413. OTTM model outputs (Valsala, 2024) used in this study can be found at https://zenodo.org/records/12544513. For additional details, the readers may contact KC (kunal.c@incois.gov.in).

References

Bakker, D. C., Alin, S. R., Becker, M., Bittig, H. C., Castaño-Primo, R., Feely, R. A., et al. (2022). Surface Ocean CO2 Atlas database version 2022 (SOCATv2022) (NCEI Accession 0253659). https://doi.org/10.25921/1h9f-nb73

Bakker, D. C., Pfeil, B., Landa, C. S., Metzl, N., O'brien, K. M., Olsen, A., et al. (2016). A multi-decade record of high-quality fCO₂ data in version 3 of the Surface Ocean CO₂ Atlas (SOCAT). *Earth System Science Data*, 8(2), 383–413.

Brewer, P. G., Wong, G. T., Bacon, M. P., & Spencer, D. W. (1975). An oceanic calcium problem? *Earth and Planetary Science Letters*, 26(1), 81–87. https://doi.org/10.1016/0012-821x(75)90179-x

Burger, F. A., & Frölicher, T. L. (2023). Drivers of surface ocean acidity extremes in an earth system model. *Global Biogeochemical Cycles*, 37(9), e2023GB007785. https://doi.org/10.1029/2023gb007785

Canadell, J. G., Monteiro, P. M., Costa, M. H., Da Cunha, L. C., Cox, P. M., Eliseev, A. V., et al. (2021). Global carbon and other biogeochemical cycles and feedbacks. Retrieved from https://oceanrep.geomar.de

Carter, B., Feely, R., Williams, N., Dickson, A., Fong, M., & Takeshita, Y. (2018). Updated methods for global locally interpolated estimation of alkalinity, pH, and nitrate. *Limnology and Oceanography: Methods*, 16(2), 119–131. https://doi.org/10.1002/lom3.10232

Chakraborty, K. (2024). A regional high-resolution (1/12 degree) coupled ocean-ecosystem model (INCOIS-BIO-ROMS) output for Indian Ocean [Dataset]. *Zenodo*. https://doi.org/10.5281/zenodo.11670413

Chakraborty, K., Kumar, N., & Gupta, G. (2017). Getting the right wind-forcing for an ecosystem model: A case study from the eastern Arabian Sea. *Journal of Operational Oceanography*, 10(2), 176–190. https://doi.org/10.1080/1755876x.2017.1354686

Chakraborty, K., Lotliker, A. A., Majumder, S., Samanta, A., Baliarsingh, S., Ghosh, J., et al. (2019). Assessment of model-simulated upper ocean biogeochemical dynamics of the Bay of Bengal. *Journal of Sea Research*, 146, 63–76. https://doi.org/10.1016/j.seares.2019.01.001

Chakraborty, K., Valsala, V., Bhattacharya, T., & Ghosh, J. (2021). Seasonal cycle of surface ocean pCO_2 and pH in the northern Indian Ocean and their controlling factors. *Progress in Oceanography*, 198, 102683. https://doi.org/10.1016/j.pocean.2021.102683

Chakraborty, K., Valsala, V., Gupta, G., & Sarma, V. (2018). Dominant biological control over upwelling on pCO_2 in sea east of Sri Lanka. *Journal of Geophysical Research: Biogeosciences*, 123(10), 3250–3261. https://doi.org/10.1029/2018jg004446

Chang, Y.-S., Zhang, S., Rosati, A., Delworth, T. L., & Stern, W. F. (2013). An assessment of oceanic variability for 1960–2010 from the GFDL ensemble coupled data assimilation. *Climate Dynamics*, 40(3–4), 775–803. https://doi.org/10.1007/s00382-012-1412-2

Chau, T. T. T., Gehlen, M., & Chevallier, F. (2022). A seamless ensemble-based reconstruction of surface ocean pCO$_2$ and air–sea CO$_2$ fluxes over the global coastal and open oceans. *Biogeosciences*, *19*(4), 1087–1109. https://doi.org/10.5194/bg-19-1087-2022

Chau, T. T. T., Gehlen, M., Metzl, N., & Chevallier, F. (2024). CMEMS-LSCE: A global, 0.25°, monthly reconstruction of the surface ocean carbonate system. *Earth System Science Data*, *16*(1), 121–160. https://doi.org/10.5194/essd-16-121-2024

Dalpadado, P., Roxy, M. K., Arrigo, K. R., van Dijken, G. L., Chierici, M., Ostrowski, M., et al. (2023). Rapid climate change alters the environment and biological production of the Indian Ocean. *Science of the Total Environment*, *906*, 167342. https://doi.org/10.1016/j.scitotenv.2023.167342

De Verneil, A., Lachkar, Z., Smith, S., & Lévy, M. (2022). Evaluating the Arabian Sea as a regional source of atmospheric CO$_2$: Seasonal variability and drivers. *Biogeosciences*, *19*(3), 907–929. https://doi.org/10.5194/bg-19-907-2022

Fennel, K., Hu, J., Laurent, A., Marta-Almeida, M., & Hetland, R. (2013). Sensitivity of hypoxia predictions for the northern Gulf of Mexico to sediment oxygen consumption and model nesting. *Journal of Geophysical Research: Oceans*, *118*(2), 990–1002. https://doi.org/10.1002/jgrc.20077

Fennel, K., Wilkin, J., Levin, J., Moisan, J., O'Reilly, J., & Haidvogel, D. (2006). Nitrogen cycling in the Middle Atlantic Bight: Results from a three-dimensional model and implications for the north Atlantic nitrogen budget. *Global Biogeochemical Cycles*, *20*(3). https://doi.org/10.1029/2005gb002456

Fennel, K., Wilkin, J., Previdi, M., & Najjar, R. (2008). Denitrification effects on air-sea CO$_2$ flux in the coastal ocean: Simulations for the northwest North Atlantic. *Geophysical Research Letters*, *35*(24). https://doi.org/10.1029/2008gl036147

Friedlingstein, P., O'sullivan, M., Jones, M. W., Andrew, R. M., Gregor, L., Hauck, J., et al. (2022). Global carbon budget 2022. *Earth System Science Data Discussions*, *2022*(11), 1–159. https://doi.org/10.5194/essd-14-4811-2022

Ghosh, J., Chakraborty, K., Chanda, A., Akhand, A., Bhattacharya, T., Das, S., et al. (2021). Outwelling of total alkalinity and dissolved inorganic carbon from the Hooghly River to the adjacent coastal Bay of Bengal. *Environmental Monitoring and Assessment*, *193*(7), 415. https://doi.org/10.1007/s10661-021-09191-y

Gregor, L., & Gruber, N. (2021). OceanSODA-ETHZ: A global gridded data set of the surface ocean carbonate system for seasonal to decadal studies of ocean acidification. *Earth System Science Data*, *13*(2), 777–808. https://doi.org/10.5194/essd-13-777-2021

Gruber, N., Clement, D., Carter, B. R., Feely, R. A., Van Heuven, S., Hoppema, M., et al. (2019). The oceanic sink for anthropogenic CO$_2$ from 1994 to 2007. *Science*, *363*(6432), 1193–1199. https://doi.org/10.1126/science.aau5153

Joshi, A. P., Chowdhury, R. R., Warrior, H. V., & Kumar, V. (2021). Influence of the freshwater plume dynamics and the barrier layer thickness on the CO$_2$ source and sink characteristics of the Bay of Bengal. *Marine Chemistry*, *236*, 104030. https://doi.org/10.1016/j.marchem.2021.104030

Joshi, A. P., Kumar, V., & Warrior, H. V. (2022). Modeling the sea-surface pCO$_2$ of the central Bay of Bengal region using machine learning algorithms. *Ocean Modelling*, *178*, 102094. https://doi.org/10.1016/j.ocemod.2022.102094

Joshi, A. P., Roychowdhury, R., Kumar, V., & Warrior, H. V. (2020). Configuration and skill assessment of the coupled biogeochemical model for the carbonate system in the Bay of Bengal. *Marine Chemistry*, *226*, 103871. https://doi.org/10.1016/j.marchem.2020.103871

Joshi, A. P., & Warrior, H. V. (2022). Comprehending the role of different mechanisms and drivers affecting the sea-surface pCO$_2$ and the air-sea CO$_2$ fluxes in the Bay of Bengal: A modeling study. *Marine Chemistry*, *243*, 104120. https://doi.org/10.1016/j.marchem.2022.104120

Keeling, C. D., Whorf, T. P., Wahlen, M., & Van der Plichtt, J. (1995). Interannual extremes in the rate of rise of atmospheric carbon dioxide since 1980. *Nature*, *375*(6533), 666–670. https://doi.org/10.1038/375666a0

Key, R. M., Kozyr, A., Sabine, C. L., Lee, K., Wanninkhof, R., Bullister, J. L., et al. (2004). A global ocean carbon climatology: Results from Global Data Analysis Project (GLODAP). *Global Biogeochemical Cycles*, *18*(4). https://doi.org/10.1029/2004gb002247

Kumar, M. D., Naqvi, S., George, M., & Jayakumar, D. (1996). A sink for atmospheric carbon dioxide in the northeast Indian Ocean. *Journal of Geophysical Research: Oceans*, *101*(C8), 18121–18125. https://doi.org/10.1029/96jc01452

Laurent, A., Fennel, K., Cai, W.-J., Huang, W.-J., Barbero, L., & Wanninkhof, R. (2017). Eutrophication-induced acidification of coastal waters in the northern Gulf of Mexico: Insights into origin and processes from a coupled physical-biogeochemical model. *Geophysical Research Letters*, *44*(2), 946–956. https://doi.org/10.1002/2016gl071881

Lauvset, S. K., Gruber, N., Landschützer, P., Olsen, A., & Tjiputra, J. (2015). Trends and drivers in global surface ocean pH over the past 3 decades. *Biogeosciences*, *12*(5), 1285–1298. https://doi.org/10.5194/bg-12-1285-2015

Lauvset, S. K., Lange, N., Tanhua, T., Bittig, H. C., Olsen, A., Kozyr, A., et al. (2021). An updated version of the global interior ocean biogeochemical data product, GLODAPv2. 2021. *Earth System Science Data Discussions*, *2021*(12), 1–32. https://doi.org/10.5194/essd-13-5565-2021

Le Quéré, C., Andrew, R. M., Friedlingstein, P., Sitch, S., Hauck, J., Pongratz, J., et al. (2018). Global carbon budget 2018. *Earth System Science Data Discussions*, *2018*(4), 1–3. https://doi.org/10.5194/essd-10-2141-2018

Le Quéré, C., Andrew, R. M., Friedlingstein, P., Sitch, S., Pongratz, J., Manning, A. C., et al. (2018). Global carbon budget 2017. *Earth System Science Data*, *10*(1), 405–448. https://doi.org/10.5194/essd-10-405-2018

Lewis, E., Wallace, D., & Allison, L. J. (1998). *Program developed for co {sub 2} system calculations (Tech. Rep.)*. Brookhaven National Lab., Dept. of Applied Science.

Li, J., Li, Y., Guo, Y., Li, G., & Wang, F. (2023). Decadal variability of sea surface salinity in the Southeastern Indian Ocean: Roles of local rainfall and the Indonesian throughflow. *Frontiers in Marine Science*, *9*, 1097634. https://doi.org/10.3389/fmars.2022.1097634

Lo Monaco, C., Metzl, N., Fin, J., Mignon, C., Cuet, P., Douville, E., et al. (2021). Distribution and long-term change of the sea surface carbonate system in the Mozambique Channel (1963–2019). *Deep Sea Research Part II: Topical Studies in Oceanography*, *186*, 104936. https://doi.org/10.1016/j.dsr2.2021.104936

Ma, D., Gregor, L., & Gruber, N. (2023). Four decades of trends and drivers of global surface ocean acidification. *Global Biogeochemical Cycles*, *37*(7), e2023GB007765. https://doi.org/10.1029/2023gb007765

Madkaiker, K., Valsala, V., Sreeush, M., Mallissery, A., Chakraborty, K., & Deshpande, A. (2023). Understanding the seasonality, trends, and controlling factors of Indian Ocean acidification over distinctive bio-provinces. *Journal of Geophysical Research: Biogeosciences*, *128*(1), e2022JG006926. https://doi.org/10.1029/2022jg006926

Metzl, N., Lo Monaco, C., Leseurre, C., Ridame, C., Fin, J., Mignon, C., et al. (2022). The impact of the south-east Madagascar bloom on the oceanic CO$_2$ sink. *Biogeosciences*, *19*(5), 1451–1468. https://doi.org/10.5194/bg-19-1451-2022

Mohanty, S., Bhattacharya, B., & Singh, C. (2024). Spatio-temporal variability of surface chlorophyll and pCO$_2$ over the tropical Indian Ocean and its long-term trend using CMIP6 models. *Science of the Total Environment*, *908*, 168285. https://doi.org/10.1016/j.scitotenv.2023.168285

Müller, J., Gruber, N., Carter, B., Feely, R., Ishii, M., Lange, N., et al. (2023). Decadal trends in the oceanic storage of anthropogenic carbon from 1994 to 2014. *AGU Advances*, *4*. https://doi.org/10.1029/2023av000875

Sabine, C., Key, R., Johnson, K., Millero, F., Poisson, A., Sarmiento, J. L., et al. (1999). Anthropogenic CO$_2$ inventory of the Indian Ocean. *Global Biogeochemical Cycles*, *13*(1), 179–198. https://doi.org/10.1029/1998gb900022

Sarma, V. V. S. S., Krishna, M., Rao, V., Viswanadham, R., Kumar, N., Kumari, T., et al. (2012). Sources and sinks of CO_2 in the west coast of Bay of Bengal. *Tellus B: Chemical and Physical Meteorology*, *64*(1), 10961. https://doi.org/10.3402/tellusb.v64i0.10961

Sarma, V. V. S. S., Kumari, V., Srinivas, T., Krishna, M., Ganapathi, P., & Murty, V. (2018). East India coastal current controls the dissolved inorganic carbon in the coastal Bay of Bengal. *Marine Chemistry*, *205*, 37–47. https://doi.org/10.1016/j.marchem.2018.07.010

Sarma, V. V. S. S., Lenton, A., Law, R., Metzl, N., Patra, P., Doney, S., et al. (2013). Sea–air CO_2 fluxes in the Indian Ocean between 1990 and 2009. *Biogeosciences*, *10*(11), 7035–7052. https://doi.org/10.5194/bg-10-7035-2013

Sarma, V. V. S. S., Sridevi, B., Metzl, N., Patra, P., Lachkar, Z., Chakraborty, K., et al. (2023). Air-Sea fluxes of CO_2 in the Indian Ocean between 1985 and 2018: A synthesis based on observations-based surface CO_2, hindcast and atmospheric inversion models. *Global Biogeochemical Cycles*, *37*(5), e2023GB007694. https://doi.org/10.1029/2023gb007694

Sarmiento, J. L. (2013). *Ocean biogeochemical dynamics*. Princeton University Press.

Sarmiento, J. L., & Gruber (2006). *Ocean biogeochemical dynamics*. Princeton University Press.

Shetye, S., Gouveia, A., Shankar, D., Shenoi, S., Vinayachandran, P., Sundar, D., et al. (1996). Hydrography and circulation in the western Bay of Bengal during the northeast monsoon. *Journal of Geophysical Research*, *101*(C6), 14011–14025. https://doi.org/10.1029/95jc03307

Sreeush, M. G., Rajendran, S., Valsala, V., Pentakota, S., Prasad, K., & Murtugudde, R. (2019). Variability, trend and controlling factors of ocean acidification over western Arabian Sea upwelling region. *Marine Chemistry*, *209*, 14–24. https://doi.org/10.1016/j.marchem.2018.12.002

Sreeush, M. G., Valsala, V., Pentakota, S., Prasad, K. V. S. R., & Murtugudde, R. (2018). Biological production in the Indian Ocean upwelling zones–part 1: Refined estimation via the use of a variable compensation depth in ocean carbon models. *Biogeosciences*, *15*(7), 1895–1918. https://doi.org/10.5194/bg-15-1895-2018

Sreeush, M. G., Valsala, V., Santanu, H., Pentakota, S., Prasad, K., Naidu, C., & Murtugudde, R. (2020). Biological production in the Indian Ocean upwelling zones-Part 2: Data based estimates of variable compensation depth for ocean carbon models via cyclo-stationary Bayesian Inversion. *Deep Sea Research Part II: Topical Studies in Oceanography*, *179*, 104619. https://doi.org/10.1016/j.dsr2.2019.07.007

Sridevi, B., & Sarma, V. V. S. S. (2021). Role of river discharge and warming on ocean acidification and pCO_2$ levels in the Bay of Bengal. *Tellus B: Chemical and Physical Meteorology*, *73*(1), 1–20. https://doi.org/10.1080/16000889.2021.1971924

Sutton, A. J., Feely, R. A., Maenner-Jones, S., Musielwicz, S., Osborne, J., Dietrich, C., et al. (2019). Autonomous seawater pCO_2$ and pH time series from 40 surface buoys and the emergence of anthropogenic trends. *Earth System Science Data*, *11*(1), 421–439. https://doi.org/10.5194/essd-11-421-2019

Sutton, A. J., Sabine, C. L., Maenner-Jones, S., Lawrence-Slavas, N., Meinig, C., Feely, R., et al. (2014). A high-frequency atmospheric and seawater pCO_2$ data set from 14 open-ocean sites using a moored autonomous system. *Earth System Science Data*, *6*(2), 353–366. https://doi.org/10.5194/essd-6-353-2014

Suzuki, T., Yamazaki, D., Tsujino, H., Komuro, Y., Nakano, H., & Urakawa, S. (2018). A dataset of continental river discharge based on JRA-55 for use in a global ocean circulation model. *Journal of Oceanography*, *74*(4), 421–429. https://doi.org/10.1007/s10872-017-0458-5

Takahashi, T., Olafsson, J., Goddard, J. G., Chipman, D. W., & Sutherland, S. (1993). Seasonal variation of CO_2 and nutrients in the high-latitude surface oceans: A comparative study. *Global Biogeochemical Cycles*, *7*(4), 843–878. https://doi.org/10.1029/93gb02263

Takahashi, T., Sutherland, S. C., Chipman, D. W., Goddard, J. G., Ho, C., Newberger, T., et al. (2014). Climatological distributions of pH, pCO_2$, total CO_2, alkalinity, and $CaCO_3$ saturation in the global surface ocean, and temporal changes at selected locations. *Marine Chemistry*, *164*, 95–125. https://doi.org/10.1016/j.marchem.2014.06.004

Takahashi, T., Sutherland, S. C., Wanninkhof, R., Sweeney, C., Feely, R. A., Chipman, D. W., et al. (2009). Climatological mean and decadal change in surface ocean pCO_2$, and net sea–air CO_2 flux over the global oceans. *Deep Sea Research Part II: Topical Studies in Oceanography*, *56*(8–10), 554–577. https://doi.org/10.1016/j.dsr2.2008.12.009

Touratier, F., Azouzi, L., & Goyet, C. (2007). CFC-11, $\Delta^{14}C$ and ^3H tracers as a means to assess anthropogenic CO_2 concentrations in the ocean. *Tellus B: Chemical and Physical Meteorology*, *59*(2), 318–325. https://doi.org/10.1111/j.1600-0889.2006.00247.x

Tsujino, H., Urakawa, S., Nakano, H., Small, R. J., Kim, W. M., Yeager, S. G., et al. (2018). JRA-55 based surface dataset for driving ocean–sea-ice models (JRA55-DO). *Ocean Modelling*, *130*, 79–139. https://doi.org/10.1016/j.ocemod.2018.07.002

UNESCO. (1969). *Discharge of selected rivers of the world*. Author.

Valsala, V. (2024). OTTM outputs used to analyze Indian Ocean acidification [Dataset]. *Zenodo*. https://doi.org/10.5281/zenodo.12544513

Valsala, V., & Maksyutov, S. (2010). A short surface pathway of the subsurface Indonesian throughflow water from the Java coast associated with upwelling, Ekman transport, and subduction. *International Journal of Oceanography*, *2010*, 1–15. https://doi.org/10.1155/2010/540783

Valsala, V., & Maksyutov, S. (2013). Interannual variability of the air–sea CO_2 flux in the north Indian Ocean. *Ocean Dynamics*, *63*(2–3), 165–178. https://doi.org/10.1007/s10236-012-0588-7

Valsala, V., Maksyutov, S., & Motoyoshi, I. (2008). Design and validation of an offline oceanic tracer transport model for a carbon cycle study. *Journal of Climate*, *21*(12), 2752–2769. https://doi.org/10.1175/2007jcli2018.1

Valsala, V., Maksyutov, S., & Murtugudde, R. (2012). A window for carbon uptake in the southern subtropical Indian Ocean. *Geophysical Research Letters*, *39*(17). https://doi.org/10.1029/2012gl052857

Valsala, V., Sreeush, M., & Chakraborty, K. (2020). The IOD impacts on the Indian Ocean carbon cycle. *Journal of Geophysical Research: Oceans*, *125*(11), e2020JC016485. https://doi.org/10.1029/2020jc016485

Van Heuven, S., Pierrot, D., Rae, J., Lewis, E., & Wallace, D. (2011). *MATLAB program developed for CO_2 system calculations* (p. 530). ORNL/CDIAC-105b.

Wafar, M., Venkataraman, K., Ingole, B., Ajmal Khan, S., & LokaBharathi, P. (2011). State of knowledge of coastal and marine biodiversity of Indian Ocean countries. *PLoS One*, *6*(1), e14613. https://doi.org/10.1371/journal.pone.0014613